



# Electrolyte/Electrode Interfaces in All-Solid-State Lithium Batteries: A Review

Yuepeng Pang<sup>1</sup> · Jinyu Pan<sup>1</sup> · Junhe Yang<sup>1</sup> · Shiyu Zheng<sup>1</sup> · Chunsheng Wang<sup>2</sup>

Received: 7 September 2020 / Revised: 27 October 2020 / Accepted: 12 December 2020  
© Shanghai University and Periodicals Agency of Shanghai University 2021

## Abstract

All-solid-state lithium batteries are promising next-generation energy storage devices that have gained increasing attention in the past decades due to their huge potential towards higher energy density and safety. As a key component, solid electrolytes have also attracted significant attention and have experienced major breakthroughs, especially in terms of Li-ion conductivity. However, the poor electrode compatibility of solid electrolytes can lead to the degradation of electrolyte/electrode interfaces, which is the major cause for failure in all-solid-state lithium batteries. To address this, this review will summarize the in-depth understanding of physical and chemical interactions between electrolytes and electrodes with a focus on the contact, charge transfer and Li dendrite formation occurring at electrolyte/electrode interfaces. Based on mechanistic analyses, this review will also briefly present corresponding strategies to enhance electrolyte/electrode interfaces through compositional modifications and structural designs. Overall, the comprehensive insights into electrolyte/electrode interfaces provided by this review can guide the future investigation of all-solid-state lithium batteries.

## 1 Introduction

The exploration of advanced lithium batteries with high energy density and excellent safety is vital for the widespread application of electric vehicles and smart grids [1]. In this regard, all-solid-state lithium batteries (ASSLBs) have recently become a research hotspot due to several key advantages, including (1) the avoidance of volatile and flammable organic liquid electrolytes; (2) the potential suppression of Li dendrite formation in electrolytes; (3) the prevention of undesirable shuttling phenomena of soluble components; (4) the possibility of applying more aggressive cathodes; and (5) the use of bipolar stacks that can simplify packaging for large-scale integration [2]. Of the various ASSLB components, solid electrolytes are key and can control overall electrochemical performance [3]. Early

investigations on the solid electrolytes mainly focused on the Li-ion conductivity, resulting in the development of many highly Li-ion conductive electrolytes, including  $\text{Li}_{3-x}\text{La}_{2/3-x}\text{TiO}_3$  [LLTO,  $10^{-4}$  S  $\text{cm}^{-1}$  at room temperature (RT)] [4],  $\text{Li}_7\text{La}_3\text{Zr}_2\text{O}_{12}$  (LLZO,  $10^{-4}$  S  $\text{cm}^{-1}$  at RT) [5],  $\text{Li}_2\text{S-P}_2\text{S}_5$  (LPS  $10^{-3}$  S  $\text{cm}^{-1}$  at RT) [6],  $\text{Li}_{10}\text{GeP}_2\text{S}_{12}$  (LGPS  $10^{-2}$  S  $\text{cm}^{-1}$  at RT) [6],  $\text{Li}_3\text{InCl}_6$  ( $10^{-3}$  S  $\text{cm}^{-1}$  at RT) [7] and  $\text{Li}_2\text{B}_{12}\text{H}_{12}$  ( $10^{-4}$  S  $\text{cm}^{-1}$  at RT) [8], all of which demonstrate Li-ion conductivities comparable to or even higher than those of commercial organic liquid electrolytes (e.g., 1 mol  $\text{L}^{-1}$   $\text{LiPF}_6$  in ethylene carbonate and dimethyl carbonate solution,  $10^{-2}$  S  $\text{cm}^{-1}$ ) [9].

In the last decade however, electrolyte/electrode interfaces have aroused increasing attention due to the fact that corresponding degradation has been found to be the main reason for ASSLB failure. For example, poor wettability, inappropriate microstructures and stress cracking can cause inferior solid–solid heterogeneous contact between electrolytes and electrodes, all of which can significantly reduce the effective interaction area of electrolyte/electrode interfaces [10]. Undesirable interphases [11] as well as resistive space charge layers [12] can lead to sluggish charge transfer between electrolytes and electrodes, both of which can remarkably increase the area specific resistance of electrolyte/electrode interfaces. These two issues can collectively lead to high internal resistances in

✉ Shiyu Zheng  
szyzheng@usst.edu.cn

✉ Chunsheng Wang  
cswang@umd.edu

<sup>1</sup> School of Materials Science and Engineering, University of Shanghai for Science and Technology, Shanghai 200093, China

<sup>2</sup> Department of Chemical and Biomolecular Engineering, University of Maryland, College Park, MD 20742, USA

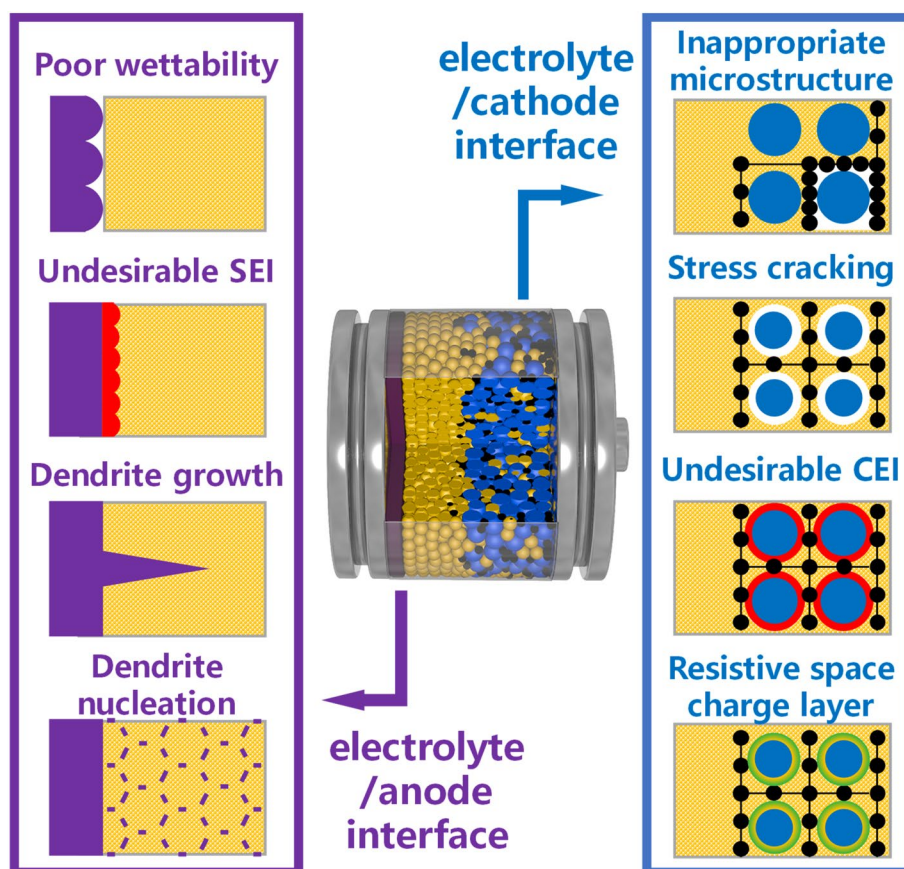
ASSLBs. Moreover, uncontrollable plating and stripping of Li during cycling can result in Li dendrites nucleation and growth at electrolyte/anode interfaces or in electrolytes, which leads to the short circuiting of ASSLBs [13].

To resolve these issues, numerous efforts have been committed to the mechanism analysis and structural optimization of electrolyte/electrode interfaces with major breakthroughs being achieved recently. Because of this, a comprehensive review is needed to understand current investigations into electrolyte/electrode interfaces in ASSLBs. And although many systematic reviews have already been published on this topic [14, 15], in-depth insights into physical and chemical interactions between electrolytes and electrodes remain lacking. To address this, this review will classify the current issues of electrolyte/electrode interfaces in ASSLBs into three categories, including poor contact, sluggish charge transfer and Li dendrite formation and focus mainly on the fundamental mechanisms of these issues (Fig. 1). This review will subsequently introduce corresponding optimization strategies and provide suggestions for future research.

## 2 Overview of Electrolyte/Electrode Interfaces

Lithium battery chemistry is based on electrochemical reactions at the electrolyte/electrode interface involving the combination of charge transport between anodic and cathodic active materials through the electrolyte (the single Li-ion conductor) and external circuits (the single electron conductor) in which to ensure the complete reaction of active materials, electrolyte/electrode structures should be well designed [16]. For Li anodes, simple layered electrolyte/Li/current collector structures are optimal because Li is electron conductive and can allow for continuous Li plating and stripping at the electrolyte/Li interface. As for other electrodes (non-Li electrodes), optimal conditions are complex due to the existence of two active material states (the lithiated state and the delithiated state) in which if the two states of an active material can, respectively, conduct Li-ions and electrons, simple layered structures can enable continuous electrochemical reaction. However, these types of active materials have yet to be found. And although some oxide-type active materials can possess certain Li-ion and electron conductivities, values are insufficient. Alternatively, alloy-type active materials generally show high electron

**Fig. 1** Current issues faced by electrolyte/electrode interfaces in ASSLBs



conductivity but low Li-ion conductivity. As a result, hierarchically interconnected microstructures are needed in optimal non-Li electrodes to ensure the complete reaction of active materials by significantly reducing Li-ion and electron transfer distances in active materials. In ASSLBs however, undesirable physical and chemical interactions at corresponding electrolyte/electrode interfaces generate large gaps between expected and actual performances.

First, poor electrolyte/electrode interfacial contact can reduce effective interaction areas. For example, many electrolytes are lithiophobic due to high interfacial energy against Li, which can lead to large contact angles ( $> 90^\circ$ ) between electrolytes and molten Li. This non-wetting phenomenon can subsequently cause poor contact and reduce effective Li-ion transfer areas between electrolytes and Li [17]. In addition, the preparation of hierarchically interconnected microstructures in non-Li electrodes is difficult and requires the precise control of the shape, size and distribution of electrolytes, active materials and electron conductors. Inappropriate microstructures can reduce the charge transfer area of electrolyte/electrode interfaces [18]. Moreover, rigid solid–solid contacts cannot accommodate active material volume change during cycling to cause significant cyclic stress. This cyclic stress can subsequently cause interfacial crack formation and propagation that will degrade the effective contact of electrolyte/electrode interfaces [19].

Second, sluggish charge transfer through electrolyte/electrode interfaces can decrease area specific resistances. For example, side reactions can occur at electrolyte/electrode interfaces if electrode working electric potentials fall outside of the electrochemical stability window of electrolytes [20]. These side reactions can irreversibly consume electrolyte and/or electrode materials to form undesirable interphases at the interface that possess high ratios of electron conductivity to Li-ion conductivity, which will allow for the further progress of side reactions and/or act as barriers to block Li-ion transfer through electrolyte/electrode interfaces [21]. Moreover, differences in Li-ion chemical potential between electrolytes and active materials can cause Li-ion redistribution regions (space charge layers) at electrolyte/electrode interfaces, which will typically result in localized Li-ion depletion layers of a certain thickness that possess low Li-ion diffusion coefficients to hinder Li-ion transfer through electrolyte/electrode interfaces [22].

Third, Li dendrite formation at electrolyte/Li interfaces or inside electrolytes can cause severe short circuiting. Here, the driving force for Li dendrite formation involves uneven electric fields as caused by inhomogeneous electrolyte/Li interfaces in which electric fields near Li protrusion are enhanced by the tip effect and nonuniform Li-ion flux [23]. Meanwhile, Li dendrite formation resistance involves extra strain energy caused by electrolyte deformation and extra interfacial energy caused by enlarged electrolyte/Li

interfaces [21]. Based on this, Li dendrite growth in electrolytes becomes spontaneous if driving forces are larger than resistive forces. In addition, ideal electrolytes are single Li-ion conductors, but current electrolytes all exhibit certain electron conductivity in which highly electron conductive electrolytes can allow for electron transfer from Li anodes towards electrolytes and reduce overall electrolyte electric potential. As a result, electrolyte electric potential during charging can lower to less than 0.0 V (vs. Li/Li<sup>+</sup>, same below), which will facilitate Li dendrite nucleation and growth inside electrolyte defects [24].

Based on this, the physical and chemical interactions at electrolyte/electrode interfaces in ASSLBs will be discussed separately in the following sections.

### 3 Electrolyte/Electrode Interfacial Contact

ASSLB electrolyte/electrode interfaces involve solid–solid contact that is significantly more complex than that in organic liquid electrolyte batteries. Here, poor electrolyte/electrode interfacial contact in ASSLBs can mainly be attributed to poor electrolyte wettability to Li, inappropriate electrolyte/electrode microstructures and stress cracking as caused by cyclic electrode volume variation, all of which can elevate the internal resistance of ASSLBs by reducing overall area for effective charge transfer.

#### 3.1 Wettability of Electrolytes to Li

The effective contact areas between electrolytes and Li in Li anodes mainly depend on electrolyte wettability to Li and can be measured by using contact angles between molten Li and electrolytes. The contact angle can be calculated by Young's equation:

$$\gamma_{\text{el/Li}} + \gamma_{\text{el/va}} \cos \theta_{\text{el/Li}} = \gamma_{\text{el/va}} \quad (1)$$

in which  $\gamma_{\text{el/Li}}$ ,  $\gamma_{\text{Li/va}}$  and  $\gamma_{\text{el/va}}$  are the interfacial energy of the electrolyte/Li interface, the Li/vapor interface and the electrolyte/vapor interface, respectively. Here, contact angles smaller than  $90^\circ$  ( $\gamma_{\text{el/Li}} < \gamma_{\text{el/va}}$ ) represent lithiophilic electrolytes that can enable the spontaneous spread of Li on electrolytes to form good contact at electrolyte/Li interfaces. Alternatively, lithiophobic electrolytes possess poor electrolyte/Li contact due to the effective contact area being much smaller than the nominal contact area.

Current investigations into the wettability of electrolytes to Li are mainly focused on LLZO, which possesses a high contact angle and therefore high apparent interfacial resistance [17]. Surface contamination in LLZO is a key factor in which Sharafi et al. [25] reported that the formation of Li<sub>2</sub>CO<sub>3</sub> and LiOH on LLZO surfaces is likely due to

exposure to air and moisture and can induce poor Li wettability (with a contact angle of  $146^\circ$ ) to cause a high interfacial resistance of  $400 \Omega \text{ cm}^2$ . In addition, these researchers reported that the removal of surface contamination through wet polishing and heat treatment can result in improved wettability (with a contact angle of  $95^\circ$ ) and a significantly reduced interfacial resistance of  $2 \Omega \text{ cm}^2$  (Fig. 2a). Based on this, lithiophilic and  $\text{Li}_2\text{CO}_3$ -free LLZO has been successfully prepared through rapid acid treatment and in situ shield protection (Fig. 2b) [26, 27]. The mechanical properties of LLZO materials are another important factor affecting wettability in which Krauskopf et al. [28] explored the electrochemical-mechanical behavior of LLZO/Li interfaces and found that high external pressures (400 MPa) can result in intimate contact and therefore interfacial resistances close to 0 (Fig. 2c). Wang et al. [29] also proposed that surface adhesion strength can quantitatively measure the wettability of electrolytes to Li at RT in which an apparent negative correlation was found between adhesion strength and interfacial resistance, which is a direct bridge between mechanical property and electrochemical performance (Fig. 2d).

Wetting properties are also strongly affected by surface chemistry because side reactions between electrolytes and Li can significantly alter interfacial properties (Sect. 4.1).

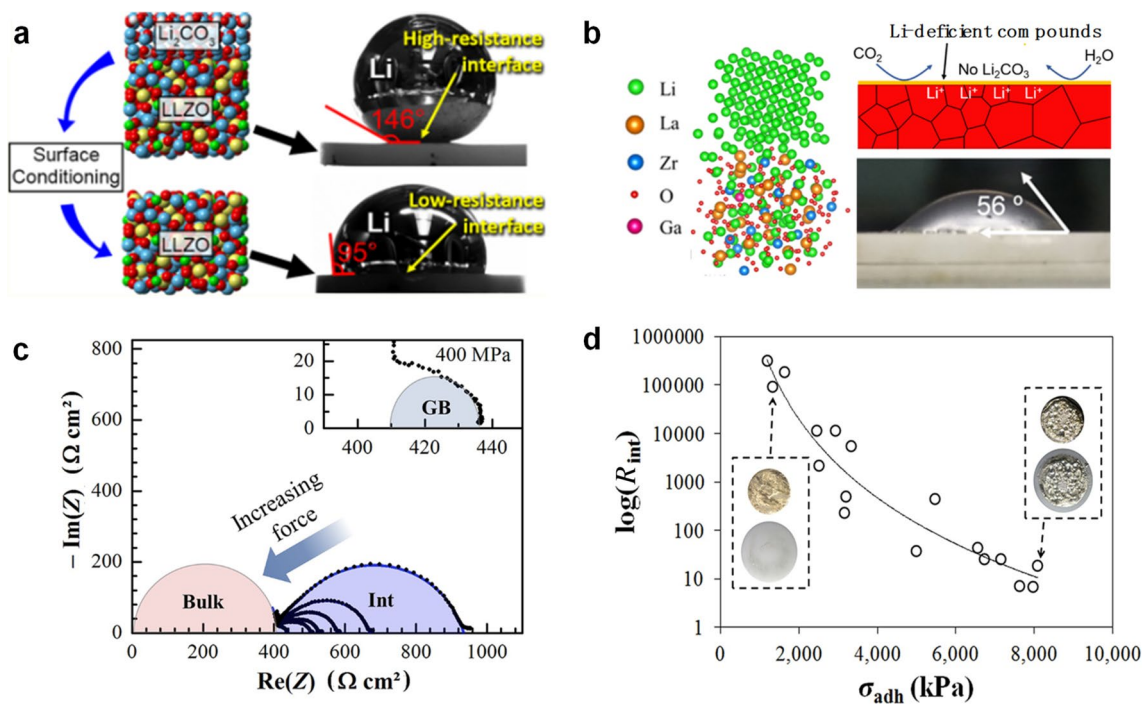


**Fig. 2** **a** Contact angles of molten Li on LLZO with and without surface contamination. Reprinted with permission from Ref. [25]. Copyright © 2017, American Chemical Society. **b** Improved wettability of Ga-doped LLZO to Li through Li-deficient compound protection. Reprinted with permission from Ref. [26]. Copyright © 2019, American Chemical Society. **c** Pressure-dependent Nyquist plots of

In addition, factors such as temperature, surface topography and electric potential can further affect wettability [30, 31] but have not yet been investigated in-depth in terms of electrolyte/Li interfaces.

### 3.2 Electrolyte and Electrode Microstructures

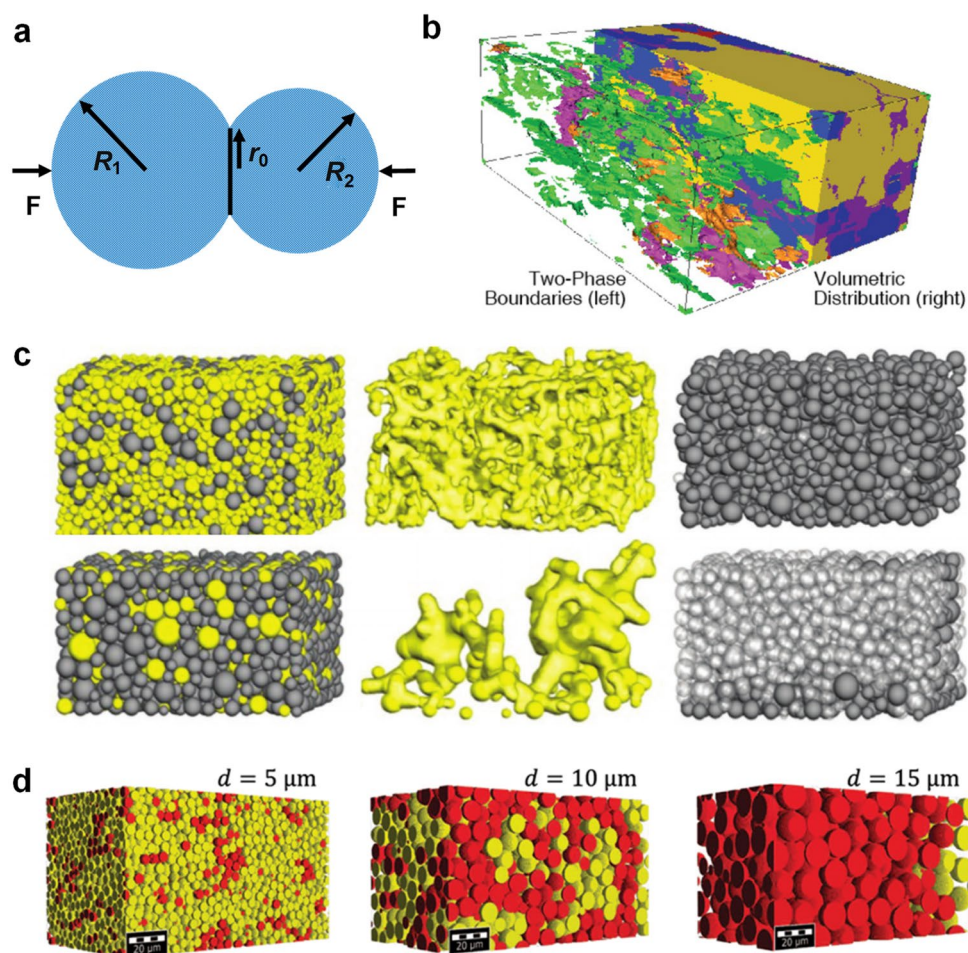
Effective contact in non-Li electrodes strongly depends on hierarchically interconnected microstructures that are closely related to the shape, size and distribution of electrolytes, active materials and electron conductors. In general, electrolytes, active materials and electron conductors are irregular particles. However, intimate contact between irregular particles is not possible due to rigidity in which the Hertz contact theory simplistically describes contact as two elastic spherical bodies of radii  $R_1$  and  $R_2$  under a squeezing force  $F$  (Fig. 3a). Here, the circular contact region radius  $r_0$  can be calculated by the following equation [32]:

$$r_0 = \left( \frac{R_1 R_2}{R_1 + R_2} \right)^{\frac{1}{3}} \frac{3}{4} F \left( \frac{1 - \nu_1^2}{E_1} + \frac{1 - \nu_2^2}{E_2} \right) \quad (2)$$

Li/LLZO/Li cells. Reprinted with permission from Ref. [28]. Copyright © 2019, American Chemical Society. **d** Relationship between the logarithm of interfacial resistance and surface adhesion strength of Li/LLZO/Li cells. Reprinted with permission from Ref. [29]. Copyright © 2018, Elsevier



**Fig. 3** **a** Contact between two elastic spherical bodies in which the spheres are squeezed together with force to form a circular contact area. Reprinted with permission from Ref. [32]. Copyright © 2006, Elsevier. **b** 3D reconstructed rendering image of a cathode showing the connectivity of each component. Reprinted with permission from Ref. [18]. Copyright © 2018, American Chemical Society. **c** Visualizations of models with different active material (grey) and electrolyte (yellow) contents and sizes. The top is a 30 wt% 3  $\mu\text{m}$  electrolyte and a 70 wt% 5  $\mu\text{m}$  active material; the bottom is a 20 wt% 8  $\mu\text{m}$  electrolyte and an 80 wt% 5  $\mu\text{m}$  active material. Reprinted with permission from Ref. [38]. Copyright © 2019, John Wiley & Sons. **d** Exemplary active material microstructures at a 55 vol% fraction with (5, 10, 15)  $\mu\text{m}$  particle diameters and respective electron connected particles (yellow) and electron unconnected particles (red). Reprinted with permission from Ref. [39]. Copyright © 2019, American Chemical Society



in which  $E_1$  and  $E_2$  are the elastic moduli and  $\nu_1$  and  $\nu_2$  are the Poisson ratios. And based on this equation, decreasing  $R$ ,  $\nu$  and  $E$  and increasing  $F$  can result in larger effective contact areas for electrolyte/electrode interfaces.

On a battery scale, the spatial distributions of electrolytes, active materials and electron conductors can further determine the quantity and quality of Li-ion and electron transfer pathways. Here, ideal distributions should fulfill two requirements: (1) the amount of active material is large enough to achieve high energy density, and (2) the electrolyte and the electron conductor are, respectively, interconnected and are in simultaneous contact with all active materials.

Direct mixing is a common approach to obtain electrolyte and electrode microstructures. However, this method often results in random distributions that cannot ensure effective contact without the precise control of relative parameters [33]. For example, Choi et al. [18] performed a 3D reconstruction technique (the focused ion beam-scanning electron microscope, FIB-SEM) to quantitatively analyze the interfacial contact area between  $\text{LiNbO}_3$ -coated  $\text{Li}(\text{Ni}_x\text{Co}_y\text{Mn}_z)\text{O}_2$  (NCM),  $(\text{Li}_2\text{S})_8(\text{P}_2\text{S}_5)_2(\text{Ni}_3\text{S}_2)$  and carbon and confirmed that the effective contact area was limited,

which they attributed to the nonuniform dispersion of active materials, agglomeration of conductive carbon and interfacial micropores (Fig. 3b). Further investigations have also shown that the amount and the particle size of electrolytes, active materials and electron conductors are key for effective contact [34–36]. For example, Kimura et al. [37] perform *operando* 3D observations of electrolyte/electrode microstructures using a combination of computed-tomography and X-ray absorption near edge structure spectroscopy and found that higher active material loadings can lead to aggregation and Li-ion and electron transfer pathway reduction. Using modeling simulations and experiment testing, Shi et al. [38] further demonstrated that active material utilization was percolation-controlled in which larger size ratios of active materials to conductors can enable higher active material loadings with effective electric contact (Fig. 3c). In another study, Bielefeld et al. [39] investigated percolation characteristics through 3D microstructural modeling using macroscopic parameters including composition, porosity, particle size and overall thickness in which corresponding results were able to provide guidelines for the design of ideal

electrolyte/electrode interfacial microstructures under given conditions (Fig. 3d).

### 3.3 Electrode Volume Change Stress

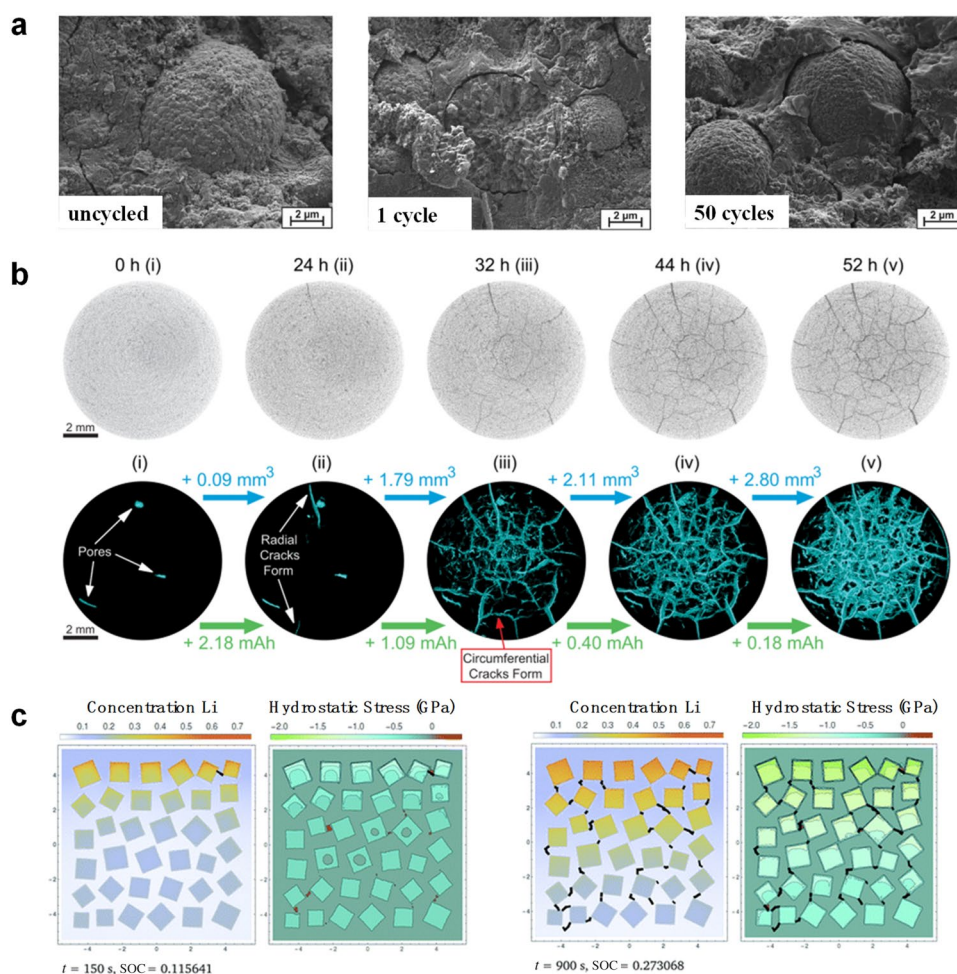
Internal stress in ASSLBs is mainly caused by the cyclical expansion and contraction of active materials. Unlike organic liquid electrolyte batteries, the stress in ASSLBs is not easily released and can cause the formation and propagation of fractures in electrolytes and/or electrodes, which can subsequently cause contact loss and result in poor Li-ion and electron transfer. Researchers have performed the direct observation of stress cracking [40, 41]. For example, Koerver et al. [19] detected stress cracking between electrolytes and NCM after cycling using SEM and attributed this to the volume change of NCM during lithiation and delithiation (Fig. 4a). Tippens et al. [42] further visualized the chemo-mechanical degradation of a  $\text{Li}_{1+x}\text{Al}_x\text{Ge}_{2-x}(\text{PO}_4)_3$  (LAGPO)/Li interface using X-ray computed tomography and found that the interactions between LAGPO and Li can lead to crack formation near the edge of the LAGPO/Li

interface (Fig. 4b). A similar phenomenon was also detected at a  $\text{Li}_{1+x}\text{Al}_x\text{Ti}_{2-x}(\text{PO}_4)_3$  (LATPO)/Li interface [43].

In terms of stress cracking suppression, external pressure is a key factor. For example, Tian et al. [44] established a relationship between applied pressure and contact area loss in  $\text{LiLiPONLiCoO}_2$  (LCO) and  $\text{LiLiGPSiTiS}_2$  cells during cycling based on Persson's contact mechanics theory and were able to determine the required pressures for contact and capacity loss recovery that agreed with experimental results.

The mechanical properties of electrolytes and electrodes can also significantly impact stress formation and relaxation in which soft electrolytes with low moduli can enhance electrolyte/electrode contact. Based on this, McGrogan et al. [45] proposed that sulfide electrolytes exhibiting lower Young's moduli and hardness than oxide electrolytes can accommodate mismatching with electrode cyclical volume change. Despite this, corresponding fracture toughness will also be much lower than that of oxide electrolytes, suggesting high sensitivity to preexisting or cycling-generated flaws. Bucci et al. [46] also conducted the quantitative analysis of mechanical reliability in ASSLBs using a coupled electro-chemo-mechanical model in which their results predicted

**Fig. 4** **a** SEM images of the cathode in an InLPS/NCM811 cell before (left), after 1 cycle (middle) and 50 cycles (right). Reprinted with permission from Ref. [19]. Copyright © 2017, American Chemical Society. **b** 2D slices of LAGPO pellets after cycling for (1) 0, (2) 24, (3) 32, (4) 44 and (5) 52 h. Dark lines represent cracks (top). Increases in crack volume and amounts of charge transfer are shown by using blue arrows and green arrows, respectively (bottom). Reprinted with permission from Ref. [42]. Copyright © 2019, American Chemical Society. **c** Li distribution and hydrostatic stress in a cathode at different stages of charge. Cracks, marked by black lines, propagate from corner to corner and cut off Li-ion diffusion pathways. Reprinted with permission from Ref. [46]. Copyright © 2017, Royal Society of Chemistry

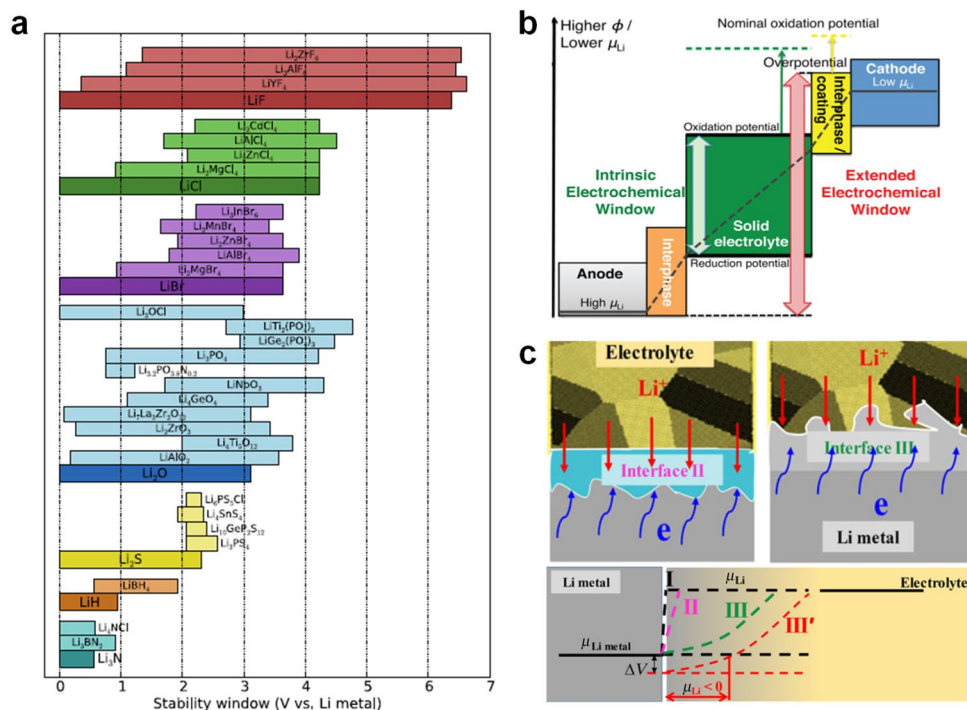




that fracture can be prevented if electrode expansion was kept at lower than 7.5% and electrolyte fracture energy was kept at higher than  $4 \text{ J m}^{-2}$ . These researchers also suggested that compliant sulfide electrolytes with Young's moduli in the order of 15 GPa resulted in greater fracture formation (Fig. 4c). And although these results are counterintuitive, they encourage in-depth investigations into the mechanical properties of electrolytes. Based on this, Deng et al. [47] predicted a series of mechanical properties such as full elastic tensors, bulk/shear/Young's moduli and Poisson's ratios of twenty-three known electrolytes using first-principle calculations that were in good agreement with existing experimental data and can serve as useful references for the design of novel electrolytes.

Battery-scale stress may further occur due to differences in the volume change ratio of active materials in which Li anodes possess infinite volume change ratios, whereas electrodes based on intercalation-type reactions possess much smaller values than those based on conversion-type reactions and alloying-type reactions. For example, Zhang et al. [48] in situ monitored pressure and height variations during the cycling of InLGPSILCO and  $\text{Li}_4\text{Ti}_5\text{O}_{12}$  (LTO)ILGPSILCO cells and reported that because both LCO and LTO were based on intercalation-type reactions, whereas metallic In was based on alloying-type reactions, corresponding pressure and height variations were much larger in the InLGPSILCO cell than in the LTOILGPSILCO cell, resulting in the direct observation of bending and cracking by X-ray tomography in the InLLCO cell due to asymmetrical volume expansion and contraction.

**Fig. 5** **a** Electrochemical stability windows of various electrolyte materials predicted by using first-principle calculations. Reprinted with permission from Ref. [51]. Copyright © 2017, American Chemical Society. **b** Electrochemical stability windows and potential profiles in ASSLBs. Reprinted with permission from Ref. [53]. Copyright © 2015, American Chemical Society. **c** Reaction and formation of an electron insulator SEI layer (left); reaction and formation of a degradation layer with high electron conductivity (right); Li potentials between Li metal and electrolytes in different interphase types (bottom). Reprinted with permission from Ref. [21]. Copyright © 2018, American Association for the Advancement of Science



## 4 Electrolyte/Electrode Interfacial Charge Transfer

Charge transfer through interfacial contact is key for ASSLB electrochemical reactions. However, Li-ion exchange between electrolytes and active materials is usually sluggish in ASSLBs and can mainly be attributed to the in situ formation of undesirable interphases from side reactions as well as resistive space charge layers as caused by potential differences between electrolytes and active materials. This sluggish charge transfer through electrolyte/electrolyte interfaces can subsequently generate high internal resistance in ASSLBs by increasing area specific resistances.

### 4.1 Interphases from Side Reactions

Electrolytes are in contact with both anodic and cathodic active materials simultaneously, which can cause side reactions if active material working electric potentials fall outside electrolyte electrochemical stability windows. And although early investigations based on cyclic voltammetry (CV) have demonstrated that many electrolytes are electrochemically stable in wide potential windows [49, 50], recent first-principle calculations have indicated that the electrochemical stability window of most electrolytes is narrower than previously claimed (Fig. 5a) [51]. For example, Han et al. [20] reported that the current signals of side reactions in conventional CV measurements using semi-block cells were too low to be observed and led to

“wider” electrochemical stability windows. These researchers subsequently added carbon into electrolytes to form LiI electrolyte/electrolyte + ClPt semi-cells to enhance contact between electrolytes and current collectors and scanned the semi-cells using CV from open-circuit voltage (OCV) to 0.0 V (to avoid large current interferences from Li plating/stripping) to obtain anodic limiting potentials and from OCV to high potentials to obtain cathodic limiting potentials. As a result, these researchers reported that the electrochemical stability windows measured using the modified semi-block cells agreed well with values from first-principle calculations, suggesting that first-principle calculations on electrochemical stability windows were accurate and can guide the estimation of side reactions between electrolytes and active materials [51–55].

Interphases (products of side reactions) can stabilize electrolyte/electrode interfaces by blocking further side reactions in which with the existence of certain interphases, electrolytes with narrow electrochemical stability windows can exhibit stable interfaces with both electrodes (Fig. 5b) [53]. Despite this, the existence of interphases also changes direct Li-ion transfer between electrolytes and active materials to indirect Li-ion transfer through the interphase, and therefore, area specific resistance is a key factor to evaluate interphases.

The ratio of electron conductivity to Li-ion conductivity in interphases plays a critical role in corresponding area specific resistance in which low electron conductivity can induce sharp potential change in interphases and therefore prevent further side reactions between electrolytes and active materials through the formation of thin interphases (Fig. 5c). Because of this, interphase thickness can be controlled by interphase electron conductivity. According to the definition of area specific resistance, the area specific resistance of interphases is positively correlated to the ratio of electron conductivity to Li-ion conductivity as shown in Eq. (3).

$$ASR_{\text{Li-ion}} = \frac{d}{\sigma_{\text{Li-ion}}} \propto \frac{\sigma_e}{\sigma_{\text{Li-ion}}} \quad (3)$$

in which  $ASR_{\text{Li-ion}}$  is the area specific resistance,  $d$  is the thickness and  $\sigma_e$  and  $\sigma_{\text{Li-ion}}$  are electron and Li-ion conductivities, respectively [21, 56, 57]. This viewpoint is well supported by both theoretical and experimental results. For example, although LiF possesses low Li-ion conductivity, it is a favorable interphase composition (Sect. 6.1) due to its extremely low electron conductivity.

LiPON is known to possess both a desirable solid electrolyte interphase (SEI) and a cathodic electrolyte interphase (CEI) that can enable ultra-high cycling stability in  $\text{Li}_{11}\text{LiNi}_{0.5}\text{Mn}_{1.5}\text{O}_4$  ASSLBs between 3.5 and 5.1 V [58]. Here, careful structural characterizations revealed that the SEI was composed of a  $\text{Li}_3\text{P}$ ,  $\text{Li}_2\text{O}$  and  $\text{Li}_3\text{N}$  mixture

in which  $\text{Li}_2\text{O}$  can contribute to low electron conductivity, whereas  $\text{Li}_3\text{N}$  can contribute to high Li-ion conductivity [59]. And although unclear, the CEI of LiPON is believed to be a  $\text{Li}_3\text{PO}_4$ -based mixture that is electron insulative and ion conductive [60]. But unfortunately, LiPON is currently the only solid electrolyte that can exhibit such excellent properties.

As for sulfide electrolytes, the reduction of LPS at low potentials can mainly be attributed to  $\text{P}^{5+}$  and will result in the formation of  $\text{Li}_2\text{S}$  and  $\text{Li}_3\text{P}$  as the SEI [61, 62]. Because  $\text{Li}_3\text{P}$  is a semiconductor with a comparable band-gap (0.70 eV) to Ge (0.66 eV) and the amount of  $\text{Li}_3\text{P}$  in LPS SEIs is higher than that in LiPON SEIs, higher electron conductivities are experienced [63]. The addition of Ge, Sn or Si elements into LPS can significantly increase Li-ion conductivity but will lead to poorer SEIs because  $\text{Ge}^{4+}$ ,  $\text{Sn}^{4+}$  and  $\text{Si}^{4+}$  can readily react with Li to form electron conductive alloys and therefore result in the continuous lithiation of electrolytes and growth of resistances [64, 65]. Sulfide electrolytes are also reactive to LCO. In terms of LPS, transmission electron microscopy (TEM) observations showed that the corresponding CEI contained Co, P and S elements with Co diffusing into LPS for over 50 nm (Fig. 6a) [66]. In addition, the main composition of the CEI was calculated to be Co–S compounds,  $\text{Li}_3\text{PO}_4$  and  $\text{Li}_2\text{SO}_4$  and is electron conductive due to the existence of Co–S compounds [67, 68]. Similar reactions also occur in LGPS/LCO interfaces [69, 70]. Alternatively, the inter-diffusion of P elements from sulfide electrolytes can be alleviated through the use of a  $\text{LiFePO}_4$  cathode that also contains  $\text{P}^{5+}$  ions [67, 71]. Furthermore, sulfide electrolytes can self-decompose to form CEIs around electron conductors (i.e., carbon), which can degrade entire Li-ion pathways and induce large resistances [72].

Oxide electrolytes can exhibit wider electrochemical stability windows. For example, the in situ scanning transmission electron microscopy (STEM) characterization of LLZO indicated the slight reduction of  $\text{Zr}^{4+}$  and the formation of an ultrathin (6 nm) tetragonal LLZO layer at the LLZO/Li interface, both of which can induce negligible area specific resistance (Fig. 6b) [73, 74]. Alternatively, the doping of Ta into LLZO does not change SEIs, whereas Fe and Nb doping can lead to thick SEIs and higher area specific resistances [75, 76]. CEI formation at LLZO/cathode interfaces mainly occurs during co-sintering due to enhancements in side reaction kinetics. And although the exact composition of CEIs at LLZO/LCO interfaces remains controversial,  $\text{La}_2\text{CoO}_4$ ,  $\text{La}_2\text{ZrO}_7$  and  $\text{Co}_3\text{O}_4$  are possible composition at different sintering temperatures due to Li loss and mutual elemental diffusion (Fig. 6c) [77–80]. And because these CEIs are all Li depleted, the fast insertion and extraction of Li-ions are restrained. Other oxide cathodes also experience similar side reactions to LLZO during sintering [81,



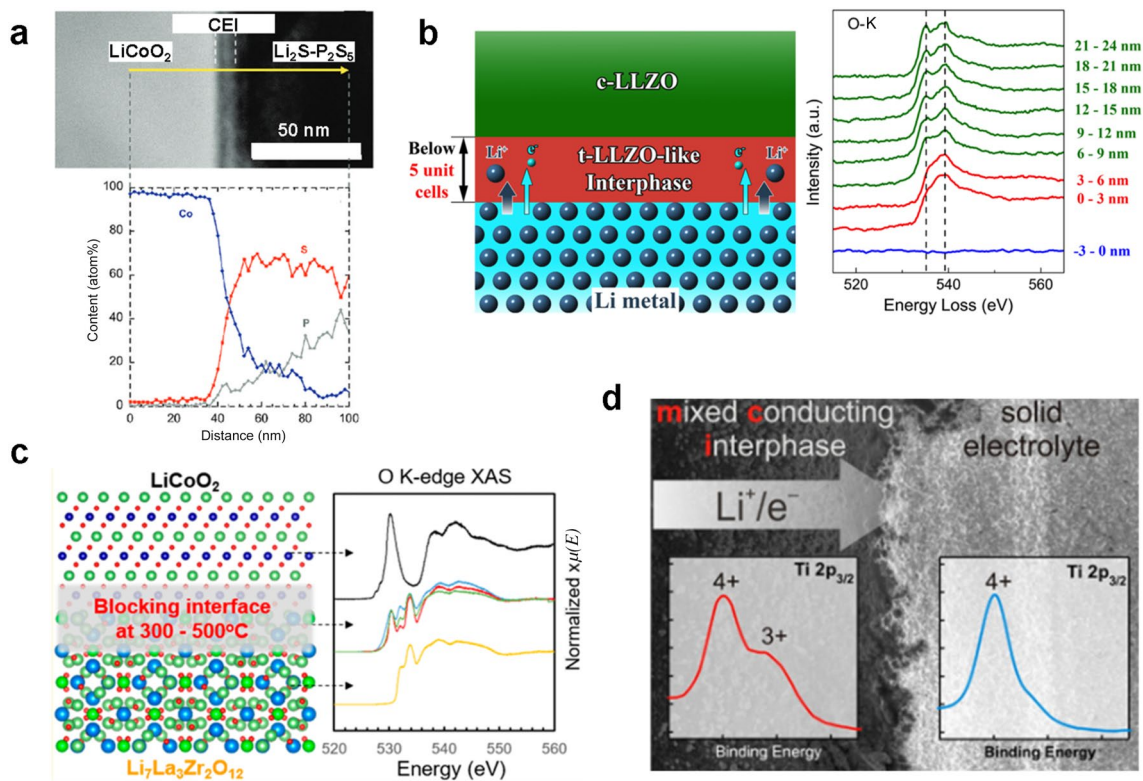


**Fig. 6** **a** Cross-sectional STEM image of an LPS/LCO interface after initial charging and energy dispersive X-ray spectroscopy line profiles for Co, P and S elements. Reprinted with permission from Ref. [66]. Copyright © 2010, American Chemical Society. **b** EELS O K-edge spectra across the LLZO/Li interface showing the formation of an ultra-thin tetragonal LLZO interphase. Reprinted with permission from Ref. [73]. Copyright © 2016, American Chemical Society.

**c** O K-edge X-ray absorption spectroscopy data across the LLZO/LCO interface showing the formation of  $\text{La}_2\text{Zr}_2\text{O}_7$ ,  $\text{Li}_2\text{CO}_3$  and  $\text{LaCoO}_3$  blocking interphases [79]. **d** XPS spectra across the LAGPO/Li interface showing the partial reduction of  $\text{Ti}^{4+}$  to  $\text{Ti}^{3+}$  in LAGPO. Reprinted with permission from Ref. [85]. Copyright © 2013, American Chemical Society

[82]. As for LLTO, it is highly reactive toward Li due to the reduction of  $\text{Ti}^{4+}$  to lower valences [83]. In addition, the SEI formed at LLTO/Li interfaces can exhibit high electron conductivity due to the existence of metallic Ti in the SEI [57]. And although LLTO is stabler at higher potentials, high-temperature sintering with LCO at 700 °C can result in the detection of  $\text{La}_2\text{Ti}_7\text{O}_2$  and  $\text{Co}_3\text{O}_4$  as the CEI, which will result in extremely low Li-ion conductivity due to Li depletion [84]. Similar to LLTO,  $\text{Ti}^{4+}$  and  $\text{Ge}^{4+}$  in LATPO and LAGPO are highly susceptible to reduction at low potentials in which the reduction products as predicted by using first-principle calculations contain Ti–Al, Li–Al and Li–Ge alloys with high electron conductivities [53]. Experimental results also support these results in which  $\text{Ge}^0$  was detected by using X-ray photoelectron spectroscopy (XPS) at the Ge-doped LATPO/Li interface (Fig. 6d) [85, 86]. And although LATPO is chemically stable to LCO even at 500 °C, interdiffusion becomes inevitable at higher temperatures and will result in the formation of a porous amorphous layer as the CEI [87].

The formation of undesirable SEIs is a major drawback in halide electrolytes in which  $\text{Li}_3\text{YCl}_6$  and  $\text{Li}_3\text{YBr}_6$  can be reduced by Li to form metallic Y containing SEIs that cannot maintain stable interfaces [88]. Alternatively, borohydride electrolytes such as  $\text{LiBH}_4$  and  $\text{Li}_2\text{B}_{12}\text{H}_{12}$  have recently been found to exhibit excellent electrochemical stability at low potentials [89, 90] in which corresponding SEIs at electrolyte/Li interfaces were thought to be a mixture of LiH and B based on first-principle calculations [51] and can possess low electron conductivity. This has however not been confirmed by experiment testing. In addition, borohydride electrolyte anions including  $[\text{BH}_4]^-$  or  $[\text{B}_{12}\text{H}_{12}]^{2-}$  contain  $\text{H}^-$  ions and are prone to oxidation. The direct contact between  $\text{LiBH}_4$  and LCO can result in high resistances after initial charging due to the formation of insulative CoO and B as a CEI [91]. And although  $\text{Li}_2\text{B}_{12}\text{H}_{12}$  is stabler, it is still incompatible with LCO and  $\text{LiFePO}_4$  cathodes due to the formation of Li-depleted CEIs [92, 93].

## 4.2 Space Charge Distribution

Space charge layers originate from the divergence of Li-ion electrochemical activity between electrolytes and electrodes. Because of this, all electrolyte/electrode interfaces should in theory possess space charge layers. However, research into interfacial space charge layers between electrolytes and Li remains scarce [94] with most focusing on interfacial space charge layers between electrolytes and cathodes.

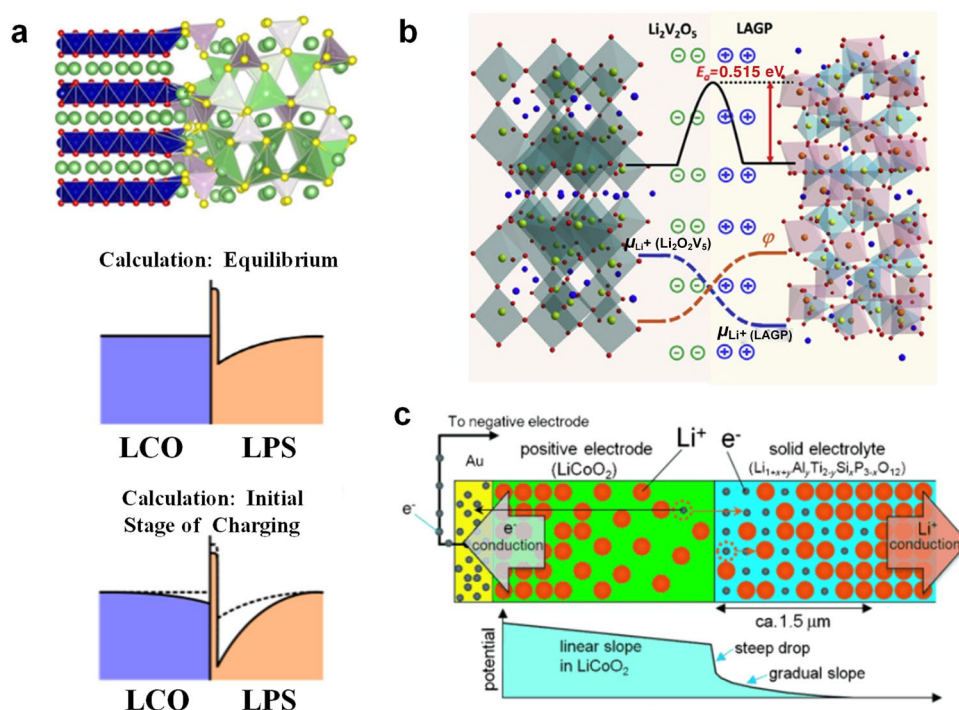
First-principle calculations indicate that Li-ions upon contact tend to transfer from LPS to LCO due to differences in Li-ion chemical potential (Fig. 7a) [22]. However, LCO is a mixed conductor that can balance Li-ion concentration gradients through electron conduction. In addition, interfacial Li atoms on LPS experience heavy adsorption to LCO surfaces, resulting in high Li-ion concentrations on this sub-layer and the formation of a Li-ion-deficient region near the sublayer to induce high resistances. During charging, the growth of space charge layers can further increase resistances in which impedances as caused by space charge layers are reported to be  $10^4 \Omega$  for LGPS/LiMn<sub>2</sub>O<sub>4</sub> and LGPS/LCO interfaces [95, 96].

Aside from sulfide electrolyte/oxide cathode interfaces, space charge layers can also exist between oxide electrolytes and oxide cathodes despite similar Li-ion attraction potentials. For example, Gittleson et al. [97] detected a Co valence increase from +3 to +4 near a Li<sub>3</sub>PO<sub>4</sub> (or LiPON)/LCO interface using XPS as caused by Li-ion transfer from LCO to Li<sub>3</sub>PO<sub>4</sub> (or LiPON) and reported that after cycling, the space charge layer grew spontaneously and therefore

exacerbated interfacial charge segregation. Fingerle et al. [60] also reported that Li-ion transfer from LCO to LiPON can result in interfacial charge redistribution and the formation of an electrostatic potential gradient as indicated by the obvious bending of the valence band, the internal electric potential profile and Li-ion electrochemical potential. Recently, Cheng et al. [98] further investigated the effects of space charge layers between Li<sub>x</sub>V<sub>2</sub>O<sub>5</sub> and LAGPO at different *x* values using 2D nuclear magnetic resonance exchange and proposed that charge separation (not Li-ion concentration) in space charge layers was responsible for significant increases in area specific resistance (Fig. 7b).

The thickness of space charge layers generally ranges from nanometers to micrometers. Here, researchers used TEM-assist electron holography coupled with electron energy loss spectroscopy (EELS) and Kelvin probe microscopy to accurately measure the space charge layer thicknesses between Si-doped LATPO and LCO and between LATPO and LiCoPO<sub>4</sub>, respectively, to propose that corresponding space charge layers were on the micrometer scale (Fig. 7c) [99, 100]. However, theoretical modeling suggested that space charge layer thicknesses between LLZO (or LATPO, LLTO) and LCO were limited to the nanometer scale by taking into consideration Coulombic interactions between defects and predicted negligible interfacial resistances [101]. This result contradicts the traditional understanding of space charge layers however and requires further experimental investigation to reveal intrinsic properties.

**Fig. 7** **a** Li concentrations at equilibrium and initial charging for an LPS/LCO interface according to first-principle calculations. Reprinted with permission from Ref. [22]. Copyright © 2014, American Chemical Society. **b** Space charge layer effects on an LAGPO/Li<sub>2</sub>V<sub>2</sub>O<sub>5</sub> interface. The space charge layer led to higher barriers for Li-ion diffusion and smaller exchange current density. Reprinted with permission from Ref. [98]. Copyright © 2020, Elsevier. **c** Li and electron distributions near an LATPO/LCO interface in the charged state (top) and typical distribution of measured potential (bottom). Reprinted with permission from Ref. [99]. Copyright © 2010, John Wiley & Sons



It is also noteworthy that some investigations in space charge layers ignore the existence of interphases at electrolyte/electrode interfaces, which may lead to inaccurate results. For example, Gao et al. [102] suggested that direct interfaces between LPS and LCO do not exist, but that interphases form between them, and therefore, space charge layers should be re-estimated.

## 5 Li Dendrite Formation at Electrolyte/Electrode Interfaces

Li dendrites were originally thought to be nonexistent in ASSLBs because solid electrolytes with high mechanical strength can suppress Li dendrite growth. However, both electrochemical experimentation and in situ observation clearly indicate Li dendrite growth and even direct nucleation in solid electrolytes during cycling, which inevitably result in the short circuiting of ASSLBs. In addition, critical current densities for Li dendrite formation in most solid electrolytes are much lower than those in organic liquid electrolytes, and therefore, Li dendrite formation has become one of the most critical issues in ASSLBs. As a research key, exact mechanisms for Li dendrite formation are complex and not yet fully understood in which Li dendrites may grow from anodes and penetrate into solid electrolytes or nucleate and grow directly in solid electrolytes.

### 5.1 Li Dendrite Growth into Electrolytes

Ideally, Li uniformly plates onto electrolyte/Li interfaces and induces the thickening of Li anodes only. However, Li dendrite growth in electrolytes directly occurs in ASSLBs under high current density. Here, the driving force for Li dendrite growth involves localized overpotential due to electrolyte/Li interface inhomogeneity in which protrusions inevitably exist that can generate enhanced electric fields and high overpotentials near the tips to result in the self-amplification of Li deposition on the protrusion tips [23]. Alternatively, two factors exist that can hinder Li dendrite growth in which the first involves electrolyte deformation due to Li dendrite growth and the generation of extra strain energy, whereas the second involves increased electrolyte/Li interface areas due to Li dendrite growth and the generation of extra interfacial energy (Fig. 8a) [21]. These two resistive forces can determine the critical overpotential of electrolytes and represent the capability for Li dendrite suppression. If Li dendrite driving forces (overpotential) are larger than resistive forces (critical overpotential), Li dendrites will spontaneously grow into electrolytes. Because of this, electrolytes should exhibit low area specific resistances to Li and homogeneous Li flux (small overpotential) as well as high mechanical strength and

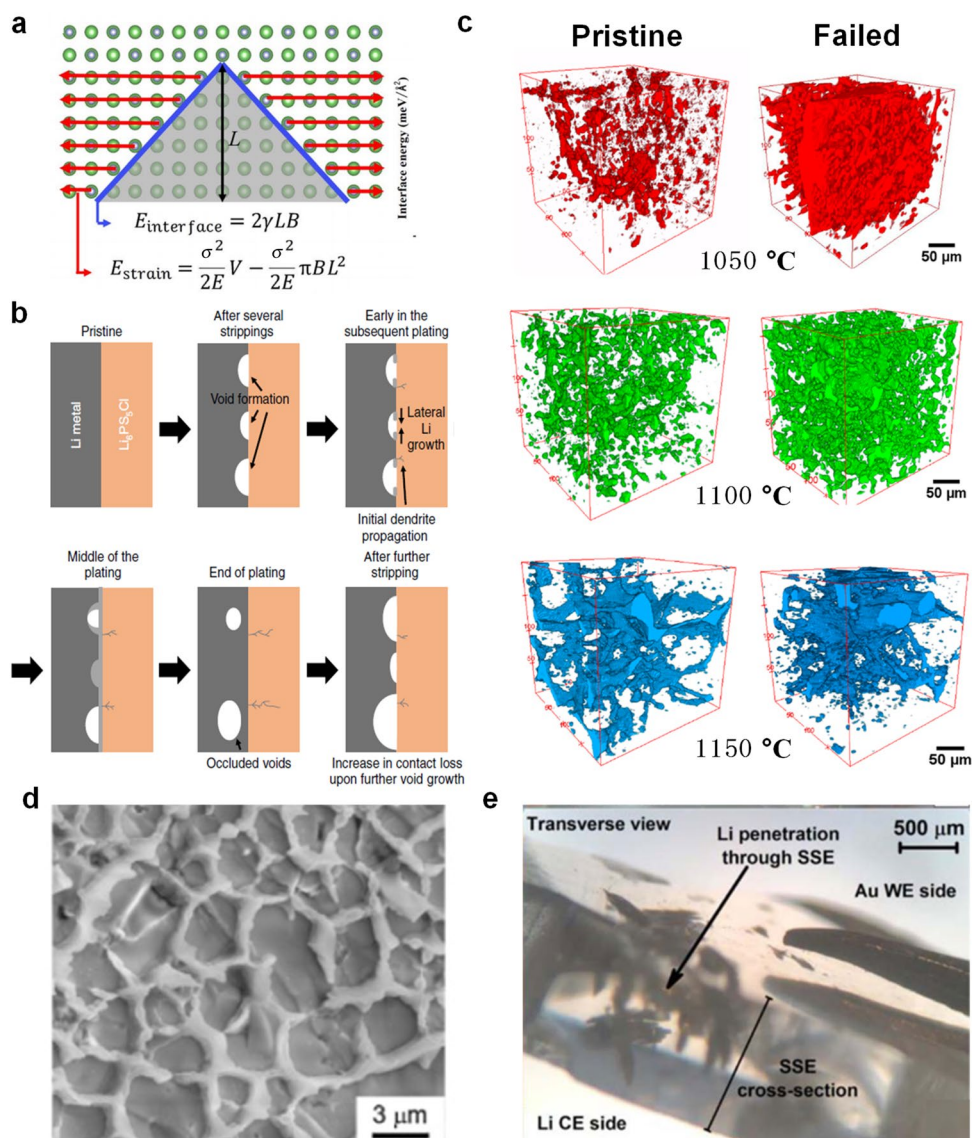
high interfacial energy against Li (large critical overpotential) to suppress Li dendrites.

In terms of Li anode inhomogeneity, this is usually caused by the poor wettability of electrolytes to Li. The resulting poor contact can not only lead to higher resistances but also the natural formation of point contacts at interfaces [103]. Poor electrolyte wettability can also cause uneven Li stripping during charging to form protrusions, resulting in point contacts that can significantly concentrate Li-ion flux distribution to result in Li dendrite formation (Fig. 8b) [104]. Here, it should be noted that the interfacial energy of electrolyte/electrode interfaces mainly determines the wettability in which high interfacial energy can lead to poor wettability (Sect. 3.1). Because of this, the effects of interfacial energy on Li dendrite suppression are contradictory in which interfacial energy is positively correlated to both the driving and resistive forces of Li dendrite growth.

In general, electrolyte inhomogeneity is caused by defects in which 3D defects such as pores and cracks play important roles in Li dendrite growth through electrolytes because corresponding pores and cracks near electrolyte/Li anode interfaces are readily filled with Li dendrites upon charging without any blocking effects [105]. Because of this, newly generated Li dendrites tend to quickly propagate to adjacent pores and cracks due to electric field amplification. For example, Shen et al. [106] directly observed the deposition of Li into the pores and cracks of LLZO to cause pore broadening and battery short circuiting (Fig. 8c). In terms of grain boundaries, these are typical 2D defects in polycrystalline electrolytes that also affect Li dendrite growth in which Cheng et al. [107] directly observed Li dendrite propagation through grain boundaries (intergranular Li dendrite formation) in Al-doped LLZO (Fig. 8d). Here, enhanced Li dendrite propagation through grain boundaries is closely related to the extraordinary properties of grain boundaries in which one reason can be ascribed to their low Li-ion conductivity and defects. For example, Yu et al. [108] examined the energetics, composition and transport properties of three low-energy symmetric model LLZO grain boundaries at the atomic scale that can represent a significant fraction of grain boundaries and reported based on molecular dynamics simulations that Li-ion transport was penalized by the higher diffusion barriers and less compact structures of grain boundaries. Ma et al. [109] further investigated the origins of poor grain boundary conductivity in LLTO using atomic-resolution STEM/EELS analysis and found that a Ti–O binary compound with a thickness of 2–3 unit cells was the actual composition of the grain boundaries and was Li depleted and therefore poorly Li-ion conductive. Here, significant differences in Li-ion conductivity between bulk grains and grain boundaries can cause inhomogeneous Li-ion flux and thus encourage Li dendrite growth. Grain boundary softening is another reason for intergranular Li dendrite growth



**Fig. 8** **a** Energy-based analysis (interfacial energy and strain energy) of Li dendrite formation. Reprinted with permission from Ref. [21]. Copyright © 2018, American Association for the Advancement of Science. **b** Schematic of an LPSC/Li interface cycled at an overall current density above critical current density for striping. Reprinted with permission from Ref. [104]. Copyright © 2019, Springer Nature. **c** X-ray tomographic reconstructions of void phases in the interior of LLZO sintered at 1050, 1100 and 1150 °C. Reprinted with permission from Ref. [106]. Copyright © 2018, American Chemical Society. **d** SEM micrographs of the web structure in cycled LLZO. Reprinted with permission from Ref. [107]. Copyright © 2017, Elsevier. **e** Transverse view showing the leaf-like morphology of Li filaments that have penetrated into or completely through single-crystal LLZO. Reprinted with permission from Ref. [112]. Copyright © 2018, The Electrochemical Society



in which Yu et al. [110] reported that the significant softening of elastic properties can occur in the nanoscale region near grain boundaries. Molecular dynamics simulations revealed that shear moduli near grain boundaries were up to 50% smaller than those in bulk regions, and therefore, Li accumulation preferentially occurs and propagates along softer grain boundary regions during charging. Elemental segregation can also cause intergranular dendrite growth. For example, Pesci et al. [111] reported that Al-doped LLZO showed much lower Li dendrite suppression capabilities than Ga-doped LLZO and that Li dendrites mainly formed through grain boundaries in Al-doped LLZO consisting of metal Li and Al, whereas for Ga-doped LLZO, no metal Ga was detected. Here, elemental distribution mapping showed that elemental Al tended to segregate at the grain boundaries in Al-doped LLZO, whereas elemental Ga distribution was homogenous in which higher concentrated Al<sup>3+</sup> at the grain

boundaries was more likely to react with Li to form Li and Al containing dendrites at the grain boundaries.

Although single-crystal LLZO is viable electrolytes for ASSLBs to minimize defect drawbacks, researchers still report obvious Li dendrite formation through in situ observations (Fig. 8e) [112–114]. In addition, researchers have reported that Li dendrite tip maximum stress as calculated using an analytical model based on simplified geometry positively correlated to overpotential in which microcrack tip pressures can easily reach 1 GPa even at normal charging rates and therefore promote crack propagation and dendrite formation until short circuiting. Zhang et al. [115] directly measured the growth stress of Li dendrites to reach 130 MPa using in situ atomic force microscopy and environmental TEM experiments. Here, the fact that higher overpotentials can induce higher stresses at Li dendrite tips confirms that overpotential is the main driving force for Li dendrite growth in ASSLBs.

## 5.2 Li Dendrite Nucleation and Growth Inside Electrolytes

Aside from the gradual growth of Li dendrites from anodes, recent studies have reported the direct nucleation and growth of Li dendrites inside electrolytes in which Aguesse et al. [116] detected Li dendrite formation inside Ga-doped LLZO and proposed two possible mechanisms based on electrochemical analysis involving (1) Li-ion reduction by  $O^{2-}$  in LLZO and (2) Li-ion reduction by electron transfer from residual electron conductivity (Fig. 9a).

Han et al. [24] reported that high electron conductivity was the origin of Li dendrite nucleation and growth inside electrolytes based on the dynamic evolution of Li concentration profiles in LiPON, LLZO and LPS during Li plating as monitored using time-resolved *operando* neutron depth profiling (Fig. 9b–d). Here, these researchers found that for LLZO and LPS, the number of cumulated Li atoms near the

anode was lower than that of transferred electrons, which suggested the formation of Li dendrites deep inside electrolytes. These researchers also found that with the exception of the anode region, the number of cumulated Li atoms was independent of depth, clearly suggesting the direct nucleation and growth of Li dendrites inside LLZO and LPS. Alternatively, LiPON can show ideal Li plating at the electrolyte/anode interface without dendrite formation inside. The main reason for these phenomena is the relatively higher electron conductivities ( $10^{-9}$ – $10^{-7}$  S  $cm^{-1}$ ) of LLZO and LPS than that of LiPON ( $10^{-15}$ – $10^{-12}$  S  $cm^{-1}$ ), which significantly reduces overall potential to negative values and promotes the inside formation of Li dendrites if directly contacting Li anodes during charging. Using a similar method, Ping et al. [117] proposed that Li nucleation and growth inside LLZO were reversible in which they found that Li dendrites can be consumed by chemical reactions with the cathode or local LLZO to fully or partially terminate short circuiting.

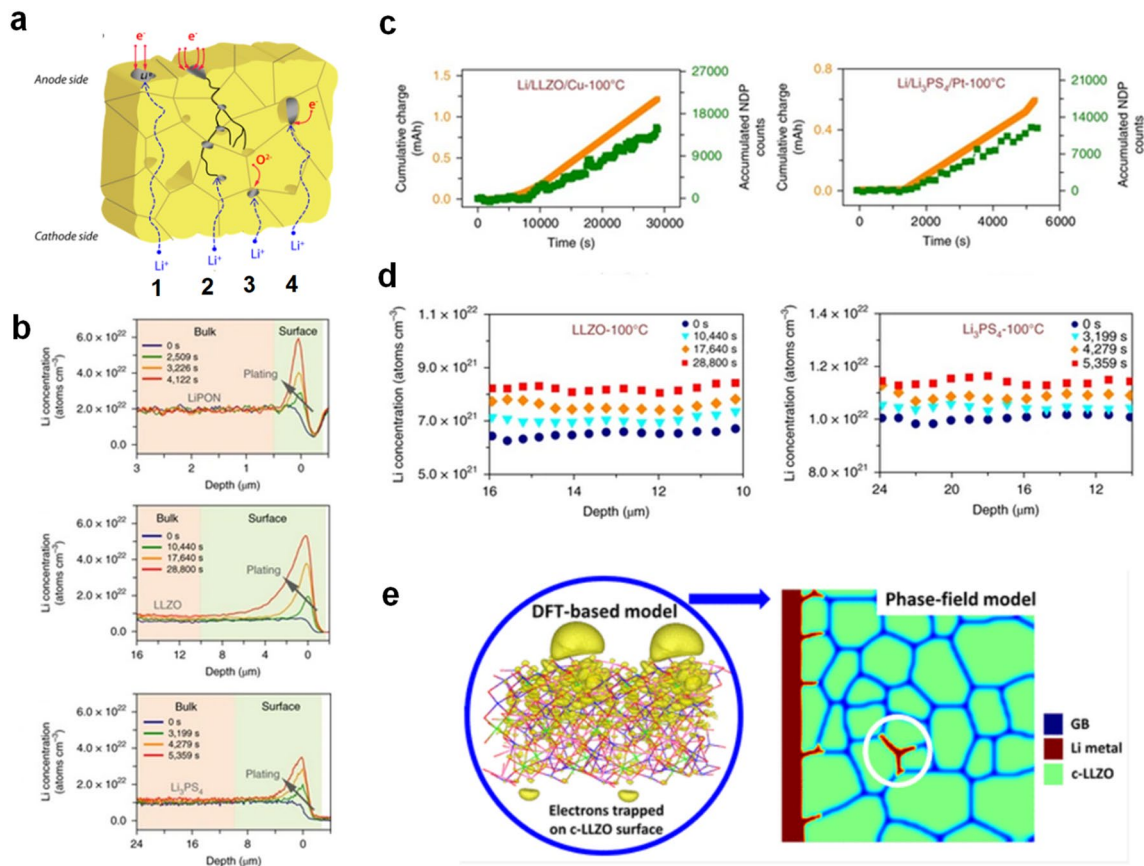
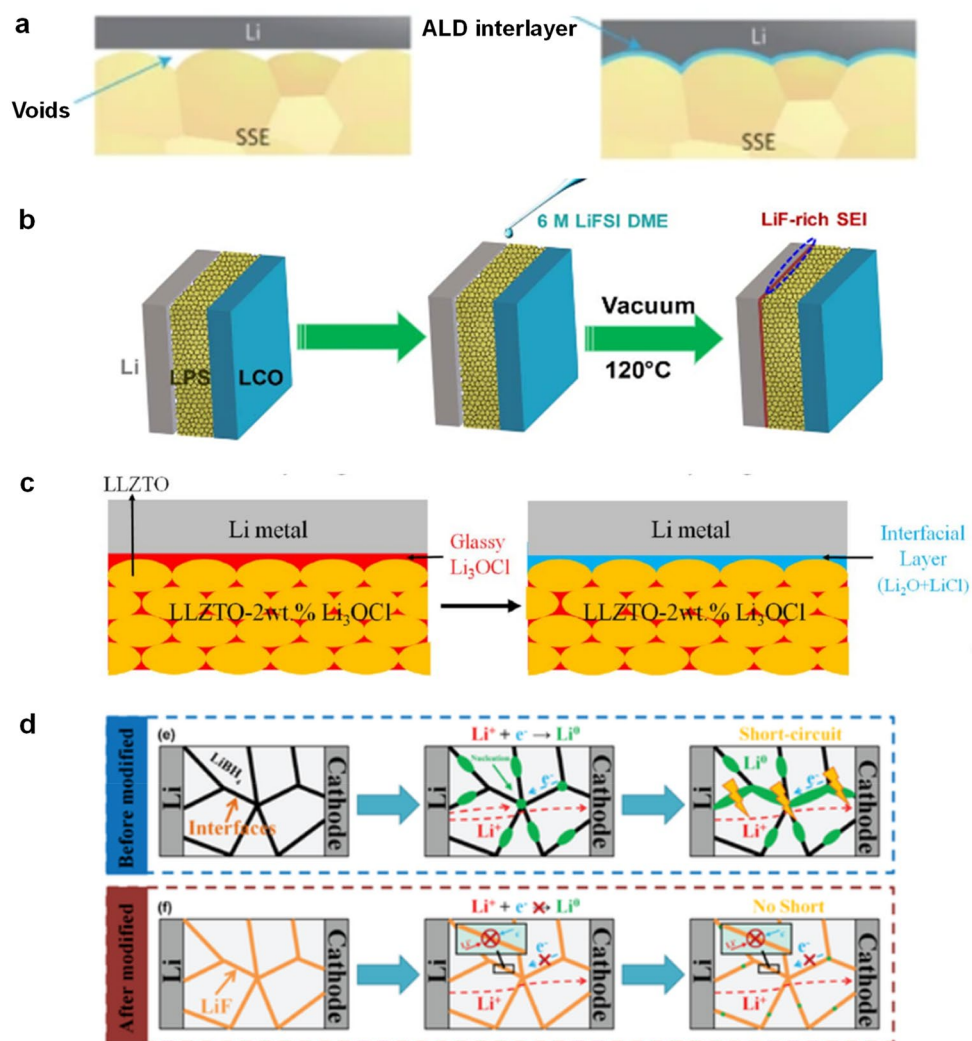


**Fig. 9** **a** Four potential Li-ion reduction mechanisms in LLZO: 1 is Li plating; 2 is Li dendrite growth; 3 and 4 are inside Li nucleation through recombination with electrons from the oxygen network and from residual electron conductivity, respectively. Reprinted with permission from Ref. [116]. Copyright © 2017, American Chemical Society. **b** Time-resolved Li concentration profiles for LCO/LiPON/Cu, Li/LLZO/Cu and Li/LPS/Pt cells. **c** Correlations between cumulative charge (the orange line) and cumulative neu-

tron depth profiling counts (green dots) in the total region (surface and bulk) of Li/LLZO/Cu and Li/LPS/Pt cells at 100 °C. **d** Li concentration profiles in LLZO and LPS at different times during Li plating. Reprinted with permission from Ref. [24]. Copyright © 2019, Springer Nature. **e** Distribution of excess electrons (the yellow region) in LLZO (left) and phase-field simulation results showing isolated dendrite nucleation (right). Reprinted with permission from Ref. [119]. Copyright © 2019, American Chemical Society

**Fig. 10** **a** Wetting behavior of garnet surfaces with molten Li before (left) and after (right) ALD modification. Reprinted with permission from Ref. [17]. Copyright © 2016, Springer Nature. **b** Pretreatment processes for the formation of a LiF-rich SEI layer between LPS and Li. Reprinted with permission from Ref. [21]. Copyright © 2018, American Association for the Advancement of Science. **c** Li deposition behaviors by using LLZO electrolytes and LLZO-2 wt%  $\text{Li}_3\text{OCl}$  composite electrolytes, formation of an interlayer between LLZO-2 wt%,  $\text{Li}_3\text{OCl}$  and Li through the *in situ* decomposition of  $\text{Li}_3\text{OCl}$ . Reprinted with permission from Ref. [133]. Copyright © 2018, Elsevier. **d** Li dendrite formation in pristine  $\text{LiBH}_4$  and Li dendrite suppression in LiF modified  $\text{LiBH}_4$ . Reprinted with permission from Ref. [138]. Copyright © 2019, John Wiley & Sons



Aside from experimental investigations, first-principle calculations can also provide insights into the nucleation and growth of Li dendrites inside electrolytes. For example, Tian et al. [118, 119] used density functional calculations and phase field simulations to propose that excess electrons can be trapped on LLZO pore surfaces due to much smaller band gaps than those in the bulk in which trapped excess electrons can accelerate Li dendrite formation and enable isolated Li nucleation inside pores (Fig. 9e).

## 6 Strategies to Improve Electrolyte/Electrode Interfaces

Practical electrolyte/electrode interfaces are more complex than ones theoretically studied in laboratory settings because multiple issues can exist and interact simultaneously. For example, poor contact and sluggish charge transfer can also play critical roles in Li dendrite formation. Despite

this, numerous successful strategies have been proposed to address the challenges of electrolyte/electrode interfaces in ASSLBs and corresponding strategies are divided and introduced according to methodology.

### 6.1 Compositional Modification

Compositional modifications of electrolyte and electrode materials can intrinsically change the properties of electrolyte/electrode interfaces in which doping, compositing and coating are three successful approaches that can improve electrolyte/electrode interfaces without lowering the Li-ion conductivity of electrolytes and the electrochemical activity of electrodes. In terms of anodes, most investigations are focused on electrolyte/Li interfaces and conclude that appropriate compositional modifications can increase wettability, form desirable SEIs and suppress Li dendrite growth. For example, the introduction of interlayers can improve the wettability of LLZO to Li in which Han et al. [17] coated



ultra-thin  $\text{Al}_2\text{O}_3$  onto Ta-doped LLZO using atomic layer deposition (ALD) to obtain a lithiophilic LLZO through the formation of Li-Al alloy (Fig. 10a). Using a similar strategy, Si, Ge, Mg, ZnO and carbon thin layers were introduced onto LLZO to successfully promote wettability [120–123]. Researchers have also reported that interlayers with high Li-ion and electron conductivities between LLZO and Li can increase wettability without hindering charge transfer. For example, Huo et al. [124] introduced a  $\text{Cu}_3\text{N}$  interlayer into LLZO using magnetic sputtering to react with Li to form a mixed conductive layer consisting of  $\text{Li}_3\text{N}$  and Cu, resulting in a decrease in apparent LLZO/Li interfacial resistance from 1138.5 to  $83 \Omega \text{ cm}^2$  and a critical current density of  $1.2 \text{ mA cm}^{-2}$ . Similarly, a  $\text{Li}_3\text{N}$ -Zn (or  $\text{Li}_3\text{N}$ -Sn) composite interlayer was successfully introduced between LLZO and Li through an in situ reaction between  $\text{Zn}(\text{NO}_3)_2$  and Li (or  $\text{SnN}_x$  and Li) [125, 126]. The formation of mixed conductive layers through electrode modification is also feasible. For example, Huang et al. [127] prepared a Li- $\text{C}_3\text{N}_4$  composite anode to decrease contact angles and suppress Li dendrite growth in which these researchers proposed that  $\text{Li}_3\text{N}$ ,  $\text{LiC}_{12}$  and  $\text{Li}_2\text{CN}_2$  in situ formed in a Li- $\text{C}_3\text{N}_4$  composite can act as the mixed conductive component. Despite these results, this strategy can only be used with relatively stable electrolytes because highly electron conductive interlayers cannot block side reactions between electrolytes and Li. In other words, although metal or alloy coating-induced wetting can reduce Li anode overpotential, it can also increase electron conductivity in which the overall impact on Li dendrite growth depends on which one plays the bigger role.

The protogenetic SEI of most electrolytes can result not only in high area specific resistances, but also in Li dendrite accumulation under certain conditions. Here, SEI engineering through modification on electrolytes and/or electrodes is a successful strategy to address this issue. For example, inspired by LiPON, O-doping in sulfide electrolytes was found to be effective in forming appropriate  $\text{Li}_2\text{O}$  containing SEIs in which the partial substitution of S with O in LGPS and  $\text{Li}_6\text{PS}_5\text{Br}$  can stabilize electrolyte/Li anode interfaces and therefore induce higher cycling stability and excellent Li dendrite suppression capability in Li|LLCO ASS-LBs [128]. Zn-O co-doped LPS and Sb-O co-doped LPS can also demonstrate better stability against Li [129, 130]. Here, it should be noted that the substitution amounts in the above studies were relatively low, which limits the  $\text{Li}_2\text{O}$  content in SEIs. Lithium halides can also form appropriate SEIs due to low electron conductivities and high interfacial energy. For example, Han et al. [131] introduced LiI into LPS to form a uniform I-doped LPS through ball milling and reported that the I-doped LPS (70LPS-30LiI) showed optimal dendrite suppression capabilities, allowing critical current densities to reach  $3.9 \text{ mA cm}^{-2}$  at  $100^\circ\text{C}$ . Here, these researchers attributed this improvement to the formation of

LiI-containing SEI. Fan et al. [21] also prepared a LiFSI-coated/infiltrated LPS in which if in contact with the Li anode, LiFSI can readily react with Li to form a LiF-rich SEI that can suppress Li dendrite penetration and increase critical current densities to  $2 \text{ mA cm}^{-2}$  at RT (Fig. 10b). Xu et al. [132] further reported that HFE (or  $\text{I}_2$ )-coated and infiltrated LPS can in situ form LiF (or LiI) rich SEIs to exhibit good Li dendrite suppression capabilities. In another study, Tian et al. [133] introduced  $\text{Li}_3\text{OCl}$  into LLZO using a melting-quenching method and reported that during cycling,  $\text{Li}_3\text{OCl}$  self-decomposed near the Li anode to form  $\text{Li}_2\text{O}$  and LiCl and that the resulting SEI was electron insulative and can adequately suppress dendrite formation (Fig. 10c).

SEI-like interlayers with low electron conductivity to Li-ion conductivity ratios have also been extensively investigated and can exhibit low area specific resistances and superior Li dendrite suppression capabilities. For example, Duan et al. [134] converted contaminants on LLZO surfaces into fluorinated interlayers at moderate temperatures to achieve high electron tunneling barriers and low energy barriers for Li-ion surface diffusion in which the LiF enriched interlayer can act as an artificial SEI to stabilize LLZO/Li interfaces. Deng et al. [135] also infused LLZO with air-stable  $\text{Li}_3\text{PO}_4$  through ALD to significantly reduce interfacial resistance to  $1 \Omega \text{ cm}^2$  and achieve a high critical current density of  $2.2 \text{ mA cm}^{-2}$  due to enhanced interfacial stability. Zhang et al. [136] further proposed that  $\text{LiH}_2\text{PO}_4$  on Li anodes can form a stable protective SEI due to reactions between  $\text{H}_3\text{PO}_4$  and Li and that the generation of this interlayer was limited due to low electron conductivity, whereas the SEI for pure LGPS grew uncontrollably. In another study, Hou et al. [137] obtained a mixture of  $\text{Li}_3\text{N}$  and LiF in situ formed through reacting Li anodes with  $\text{LiNO}_3$  and fluoroethylene carbonate and reported that the robust LiF and  $\text{Li}_3\text{N}$  containing interlayer enabled uniform Li deposition without dendrite formation in LAGPO.

Electrolyte modifications to further decrease residual electron conductivity are important to suppress dendrite formation inside electrolytes. Based on this, Mo et al. [138] modified the grain boundaries of  $\text{LiBH}_4$  through LiF doping to successfully reduce overall electron conductivity by hindering electron transfer along the grain boundaries (Fig. 10d). Using a similar strategy, Shi et al. [93] in situ prepared LiF decorated  $\text{Li}_2\text{B}_{12}\text{H}_{12}$  through a solid-state reaction in which ultra-fine LiF nanoparticles can block electron transfer and enable Li-ion migration to suppress Li dendrite nucleation inside the electrolyte and side reactions between the electrolyte and the electrode.

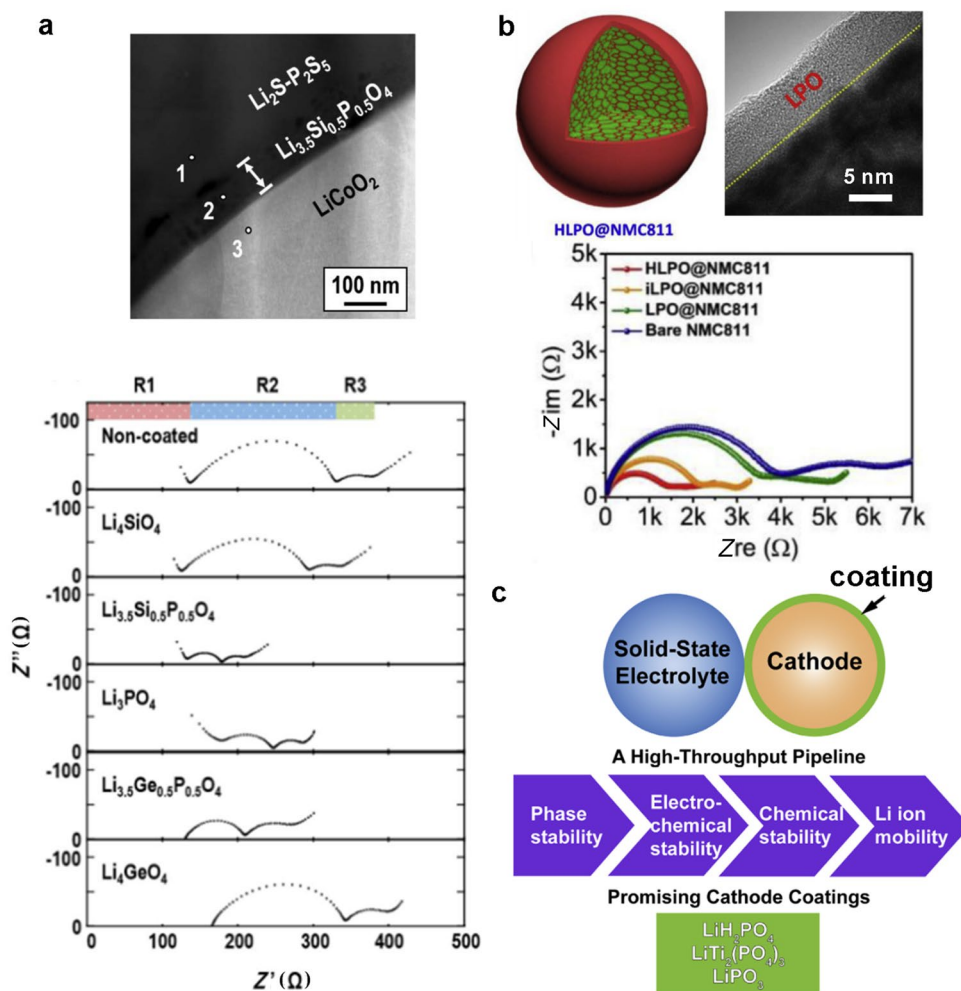
As for cathodes, compositional modifications are mainly focused on interlayer coatings to prevent side reactions and alleviate space charge layers. For example, Ohta et al. [139] coated LTO as an interlayer between LPS and LCO to successfully prevent side reactions and

reduce interfacial resistances in which because the electrochemical stability window of LTO is from 2.0 to 3.8 V, LTO is relatively stable to both LPS and LCO. In addition, LTO possesses acceptable Li-ion and electron conductivities. Following this work, LTO interlayers were also applied in the interfaces between LGPS electrolyte and  $\text{LiNi}_{0.8}\text{Co}_{0.15}\text{Al}_{0.05}\text{O}_2$ , NCM and  $\text{LiMn}_2\text{O}_4$  cathodes [140–142]. Using a similar strategy, Ohta et al. [143] developed a  $\text{LiNbO}_3$  interlayer that exhibited better performance in which  $\text{LiNbO}_3$  possesses a wide electrochemical stability window of 1.7–4.2 V, a Li-ion conductivity of  $10^{-5} \text{ S cm}^{-1}$  in the amorphous phase and an electron conductivity of  $10^{-11} \text{ S cm}^{-1}$ . As a result,  $\text{LiNbO}_3$  has been widely used as a typical interlayer [144–147]. Jung et al. [148] also rationally designed a Li–B–C–O interlayer to stabilize a  $\text{Li}_6\text{PS}_4\text{Cl}$  (LPSCl)/LCO interface in which the Li–B–C–O interlayer was formed by reactions between  $\text{Li}_3\text{BO}_3$  and  $\text{Li}_2\text{CO}_3$  (impurities on the LCO surface) and can allow for significantly enhanced Li-ion conductivity as well as the suppressed formation of detrimental  $\text{Co}_3\text{S}_4$ -containing CEIs.  $\text{Li}_3\text{PO}_4$  has been shown

to be an appropriate CEI in investigations into LiPON. Because of this,  $\text{Li}_3\text{PO}_4$  interlayer coatings are expected to effectively improve performance. For example, Ito et al. [149] deposited a  $\text{Li}_{3.5}\text{Si}_{0.5}\text{P}_{0.5}\text{O}_4$  thin film onto LCO using pulsed laser deposition and achieved much lower interfacial resistances in a corresponding InLPS/LCO cell with a 45-nm  $\text{Li}_{3.5}\text{Si}_{0.5}\text{P}_{0.5}\text{O}_4$  interlayer between LPS and LCO (Fig. 11a).  $\text{Li}_3\text{PO}_4$  interlayers have further been applied in LGPS/NCM (Fig. 11b) [150] and  $\text{LiBH}_4$ /LCO interfaces [91] with promising results. To further explore potential interlayers with favorable properties, Xiao et al. [151] conducted the high-throughput screening of electrode/cathode interlayers using first-principle calculations and predicted three new interlayers including  $\text{LiH}_2\text{PO}_4$ ,  $\text{LiTi}_2(\text{PO}_4)_3$  and  $\text{LiPO}_3$  that can potentially improve compatibility between electrolytes and cathodes (Fig. 11c).

The composition of two Li-ion conductors to form dual layer electrolytes is another effective strategy to improve interfacial compatibility. For example, Wan et al. [152] proposed an O-doped LPS/LGPS dual layer electrolyte to enable stable cycling in a  $\text{Li}_{11}\text{Cu}_2\text{ZnSnS}_4$  cell in which O-doped

**Fig. 11** **a** Cross-sectional TEM image of an InLPS/ $\text{Li}_{3.5}\text{Si}_{0.5}\text{P}_{0.5}\text{O}_4$ -coated LCO cell (top); impedance plots of ASSLBs using LCO cathodes with and without coating after initial charging (bottom). Reprinted with permission from Ref. [149]. Copyright © 2015, The Electrochemical Society. **b** Structure and characterization of hierarchical  $\text{Li}_3\text{PO}_4$ @NCM811 (top); impedance plots of ASSLBs using NCM811 with and without coating after 100 cycles. Reprinted with permission from Ref. [150]. Copyright © 2020, Elsevier. **c** Specific recommendations of coating materials obtained by high-throughput screening and detailed case studies. Reprinted with permission from Ref. [151]. Copyright © 2019, Elsevier



LPS was used at the Li anode to prevent the reduction reaction of LGPS. This dual layer electrolyte can also be used in high-performance LillS ASSLBs [153]. In another study, Lu et al. [154] applied a  $\text{Li}_4(\text{BH}_4)_3\text{I}@\text{SBA-15}/\text{LPS}$  dual layer electrolyte in a LillCO ASSLB in which the addition of LPS in electrolytes can lead to relatively stable electrolyte/electrode interfaces without severe side reactions during cycling.

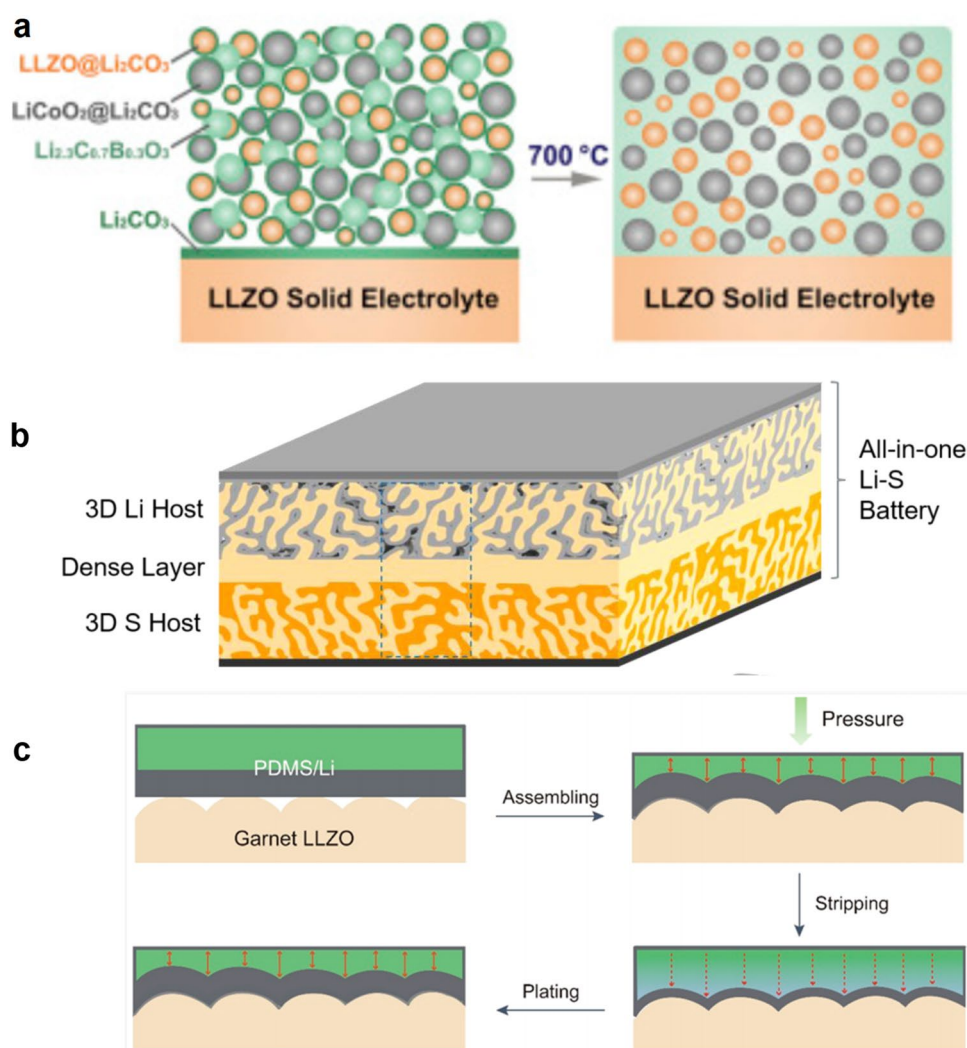
## 6.2 Structural Design

The main purpose of structural design is to form 3D intimate electrolyte/electrode interfaces to increase effective interaction areas and accommodate volume change, all of which can decrease internal resistance and suppress crack-induced short circuiting.

One effective strategy involves the solidification of liquid phases (melting–cooling or dissolving–drying) to improve interfacial contact. Using the melt–cooling strategy, Ohta et al. [155] introduced  $\text{Li}_3\text{BO}_3$  to improve the

contact between Nb-doped LLZO and LCO in which in the co-sintering process,  $\text{Li}_3\text{BO}_3$  can melt to enhance interaction with both Nb-doped LLZO and LCO. Han et al. [156] further demonstrated the soldering of LLZO and LCO through the reaction between  $\text{Li}_{2.3}\text{C}_{0.7}\text{B}_{0.3}\text{O}_3$  and  $\text{Li}_2\text{CO}_3$  (impurities on both LLZO and LCO surfaces) in which the in situ formed Li-C-B-O compound can not only induce a high interaction area, but also improve Li-ion transfer by removing insulative  $\text{Li}_2\text{CO}_3$  (Fig. 12a). Kitaura et al. [157] also fabricated a favorable electrolyte/electrode interface by hot-pressing supercooled liquid-state LPS onto LTO and LCO. Intimate contact was achieved due to the deformation of soft LPS, which significantly decreased interfacial resistance and enabled stable cycling. Melting–cooling of active materials is also effective to enhance Li-ion and electron transfer. Hou et al. [158] rationally designed a cathode structure in a LillS ASSLB by melting and infiltrating S into coaxial carbon nanotubes in which the resulting electronic network enabled high S utilization and excellent electrochemical performance.

**Fig. 12** **a** The interphase-engineered all-ceramic electrolyte/cathode interface. Reprinted with permission from Ref. [156]. Copyright © 2018, Elsevier. **b** The working principle of an all-in-one solid-state LillS battery based on the tri-layer garnet electrolyte. Reprinted with permission from Ref. [162]. Copyright © 2018, Elsevier. **c** Intimate contact between LLZO and Li as enabled by the hyper-elastic substrate PDMS. Reprinted with permission from Ref. [167]. Copyright © 2020, American Chemical Society





Using the dissolving–drying strategy, Kim et al. [159] proposed a new scalable method to achieve excellent contact between electrolytes and electrodes in which electrolyte solutions (LiPSCl in ethanol or  $0.4\text{LiI}-0.6\text{Li}_4\text{SnS}_4$  in methanol) were infiltrated into electrodes and solidified under vacuum. The corresponding graphite|LPSCl|LLCO ASSLB showed comparable electrochemical performance to organic liquid electrolyte batteries. Li et al. [160] further designed a novel electrolyte structure with LPSCl infusion into well-aligned wood channels to suppress Li dendrite formation and reported that this unique electrolyte structure led to regulated Li-ion flux and facilitated homogenous Li plating and stripping behaviors.

Porous electrolytes or electrodes possess high specific areas and are therefore expected to show high interaction areas. Based on this, van den Broek et al. [161] developed a nanoporous Al-doped LLZO which was obtained through co-sintering with a sacrificial organic temperate and the cathode was casted to achieve high interaction areas. Xu et al. [162] also developed a novel porous-dense-porous tri-layer LLZO that provided interconnected 3D Li-ion pathways throughout the entire cell, allowing a corresponding LillS ASSLB to demonstrate high energy density ( $272\text{ Wh kg}^{-1}$ ) and coulombic efficiency (nearly 100%) (Fig. 12b). Li et al. [163] further designed a 3D porous current collector to deposit Li without incurring volume expansion in which the majority of Li can successfully congregate into the void spaces of the current collector upon charging. These researchers did report however that the degradation of the electrolyte/Li interface was still inevitable due to the existence of rare interfacial Li plating. Porous electrodes can also show improved electrochemical performance. For example, Han et al. [164] synthesized porous In and Sn anodes with continuous porosity through the chemical dealloying of Li–In and Li–Sn alloys, respectively, and reported that these porous metal anodes can exhibit improved capacity and cycle lifes due to improved volume change accommodation and minimized side reactions.

Various novel ASSLB structures can better accommodate cyclical stress. For example, Han et al. [165] demonstrated a proof of concept of a single-material battery with the aim of eliminating interfacial resistance in which LGPS acted as the anode (Ge–S components with C), the electrolyte (LGPS) and the cathode (Li–S components with C). As a result, this novel structure remarkably improved solid–solid contact and can be applied to other battery chemistry. Lee et al. [166] designed an Ag–C |LPSCl|NCM ASSLB with no excess Li and reported that the thin Ag–C layer can effectively regulate Li deposition to lead to high cycling stability, allowing a prototype pouch cell to display high energy density ( $> 900\text{ Wh L}^{-1}$ ). Hyper-elastic substrates for Li anodes can also accommodate stress. For

example, Zhang et al. [167] prepared a stress self-adaptable LLZO/Li interface by integrating Li foil with a polydimethylsiloxane substrate to achieve a long cycling life of over 5000 cycles with small overpotentials (Fig. 12c).

## 7 Conclusion and Outlook

Overall, this review has presented current understandings of key issues in terms of electrolyte/electrode interfaces in ASSLBs as well as representative strategies with a focus on poor contact, sluggish charge transfer and Li dendrite formation.

In terms of poor contact, this is mainly caused by poor wettability, inappropriate microstructures and stress cracking and can result in insufficient effective interaction areas between electrolytes and electrodes. Here, poor Li wettability in electrolytes is due to the high interfacial energy of electrolytes to Li, which can lead to smaller contact areas. Alternatively, inappropriate microstructures can result in the lack of direct contact between active materials, electrolytes and electron conductors and are strongly dependent on the corresponding shape, particle size and spatial distribution. As for stress cracking, this is generated by active material cyclic volume change during cycling, which can cause contact loss and hinder Li-ion and electron transfer. To resolve these issues, successful strategies include interlayer coatings (e.g., deposition of Li containing alloys) that can improve wettability by tailoring electrolyte/Li interfacial energy as well as interfacial structural designs (e.g., solidification of liquid phases, introduction of continuous pores) that can optimize 3D conductive networks and accommodate cyclical volume change during cycling. In addition, future studies should focus on (1) achieving intimate electrolyte/Li contact without the introduction of highly electron conductive interlayers; (2) designing effective Li-ion and electron transfer pathways in high areal loading electrodes; and (3) designing controllable porous structures to accommodate volume change during cycling.

As for sluggish charge transfer, this is mainly a result of undesirable interphases and space charge layers and can result in large area specific resistances of electrolyte/electrode interfaces. Here, interphases are in situ formed through side reactions between electrolytes and electrodes in which the ratio of electron conductivity to Li-ion conductivity in interphases is key to determining area specific resistance. Alternatively, space charge layers are a result of Li-ion chemical potential differences between electrolytes and active materials and the effect mechanisms of space charge layers remain unclear. The key point is whether Li-ion redistribution can generate Li depletion regions and whether these regions can hinder Li-ion transfer. Successful strategies to obtain desirable interphases and improve

space charge layers involve artificial interphase design (e.g.,  $\text{Li}_2\text{O}$ ,  $\text{LiF}$ ,  $\text{LiI}$  and  $\text{LiCl}$  enrichment) and interlayer introduction (e.g.,  $\text{LTO}$ ,  $\text{LiNbO}_3$  and  $\text{Li}_3\text{PO}_4$  coating) and future studies should focus on (1) the development of electrolytes with the appropriate SEIs and CEIs to enable practical high energy density ASSLBs; (2) the introduction of Li-ion conductive and electrochemically stable interlayers that can alleviate resistances; and (3) the understanding of space charge layer intrinsic properties and their effect mechanisms on area specific resistance.

Lastly, Li dendrite formation is based on complex physical and chemical interactions between electrolytes and electrodes in which Li dendrites can grow into electrolytes and/or nucleate and grow inside electrolytes. Corresponding electrical field amplification near Li protrusion tips and non-uniform Li-ion flux can further stimulate Li dendrite growth, whereas extra interfacial energy and strain energy can hinder Li dendrite growth. Moreover, the nucleation and growth of Li dendrites inside electrolytes can mainly be attributed to the relatively high electron conductivity and excess surface-trapped electrons of electrolytes. Here, the interfacial energy of electrolyte/Li interfaces plays a key role, which can affect both Li dendrite driving force and resistive force. Consequently, different modification strategies (e.g., forming lithiophilic or lithiophobic interfaces) should be applied under different conditions to suppress Li dendrite growth from anodes. As for the internal nucleation and growth of dendrites, the reduction of electrolyte electron conductivity (e.g., introduction of interphases with low ratios of electron conductivity to Li-ion conductivity) has proven to be effective. Based on this, future research should focus on (1) revealing the contradictory effects of interfacial energy on dendrite suppression; (2) forming self-healing SEIs that can ensure interfacial stability even with occasional dendrite penetration; and (3) investigating potential distributions in interfaces to better understand Li dendrite formation.

**Acknowledgements** The authors gratefully acknowledge the support of the National Natural Science Foundation of China (51671135, 51971146, 51971147), the Major Program for the Scientific Research Innovation Plan of Shanghai Education Commission (2019-01-07-00-07-E00015), the Program of Shanghai Subject Chief Scientist (17XD1403000), the Shanghai Outstanding Academic Leaders Plan, the Shanghai Rising-Star Program (20QA1407100) and the General Program of Natural Science Foundation of Shanghai (20ZR1438400).

**Author contributions** SZ and CW proposed the idea for this review. YP and JP performed the literature search and data analysis, YP wrote the first draft of this review, and JY, SZ and CW revised this review.

## Compliance with ethical standards

**Conflicts of interest** The authors declare no conflicts of interest.

## References

1. Chu, S., Majumdar, A.: Opportunities and challenges for a sustainable energy future. *Nature* **488**, 294–303 (2012). <https://doi.org/10.1038/nature11475>
2. Manthiram, A., Yu, X.W., Wang, S.F.: Lithium battery chemistries enabled by solid-state electrolytes. *Nat. Rev. Mater.* **2**, 1–16 (2017). <https://doi.org/10.1038/natrevmats.2016.103>
3. Zheng, F., Kotobuki, M., Song, S.F., et al.: Review on solid electrolytes for all-solid-state lithium-ion batteries. *J. Power Sources* **389**, 198–213 (2018). <https://doi.org/10.1016/j.jpowsour.2018.04.022>
4. Sun, Y.D., Guan, P.Y., Liu, Y.J., et al.: Recent progress in lithium lanthanum titanate electrolyte towards all solid-state lithium ion secondary battery. *Crit. Rev. Solid State Mater. Sci.* **44**, 265–282 (2019). <https://doi.org/10.1080/10408436.2018.1485551>
5. Wang, C.W., Fu, K., Kammampata, S.P., et al.: Garnet-type solid-state electrolytes: materials, interfaces, and batteries. *Chem. Rev.* **120**, 4257–4300 (2020). <https://doi.org/10.1021/acs.chemrev.9b00427>
6. Lau, J., DeBlock, R.H., Butts, D.M., et al.: Sulfide solid electrolytes for lithium battery applications. *Adv. Energy Mater.* **8**, 1800933 (2018). <https://doi.org/10.1002/aenm.201800933>
7. Li, X.N., Liang, J.W., Yang, X.F., et al.: Progress and perspectives on halide lithium conductors for all-solid-state lithium batteries. *Energy Environ. Sci.* **13**, 1429–1461 (2020). <https://doi.org/10.1039/c9ee03828k>
8. Cuan, J., Zhou, Y., Zhou, T.F., et al.: Borohydride-scaffolded Li/Na/Mg fast ionic conductors for promising solid-state electrolytes. *Adv. Mater.* **31**, 1803533 (2019). <https://doi.org/10.1002/adma.201803533>
9. Xu, K.: Electrolytes and interphases in Li-ion batteries and beyond. *Chem. Rev.* **114**, 11503–11618 (2014). <https://doi.org/10.1021/cr500003w>
10. Wang, P., Qu, W.J., Song, W.L., et al.: Electro-chemo-mechanical issues at the interfaces in solid-state lithium metal batteries. *Adv. Funct. Mater.* (2019). <https://doi.org/10.1002/adfm.20190950>
11. Xiao, Y.H., Wang, Y., Bo, S.H., et al.: Understanding interface stability in solid-state batteries. *Nat. Rev. Mater.* **5**, 105–126 (2020). <https://doi.org/10.1038/s41578-019-0157-5>
12. Tateyama, Y., Gao, B., Jalem, R., et al.: Theoretical picture of positive electrode–solid electrolyte interface in all-solid-state battery from electrochemistry and semiconductor physics viewpoints. *Curr. Opin. Electrochem.* **17**, 149–157 (2019). <https://doi.org/10.1016/j.coelec.2019.06.003>
13. Cao, D.X., Sun, X., Li, Q., et al.: Lithium dendrite in all-solid-state batteries: growth mechanisms, suppression strategies, and characterizations. *Matter* **3**, 57–94 (2020). <https://doi.org/10.1016/j.matt.2020.03.015>
14. Lim, H.D., Park, J.H., Shin, H.J., et al.: A review of challenges and issues concerning interfaces for all-solid-state batteries. *Energy Storage Mater.* **25**, 224–250 (2020). <https://doi.org/10.1016/j.ensm.2019.10.011>
15. Xu, X.L., Hui, K.S., Hui, K.N., et al.: Recent advances in the interface design of solid-state electrolytes for solid-state energy storage devices. *Mater. Horiz.* **7**, 1246–1278 (2020). <https://doi.org/10.1039/c9mh01701a>
16. Allen, J.B., Larry, R.K.: *Electrochemical methods: fundamentals and applications*. Wiley, New York (2001)
17. Han, X.G., Gong, Y.H., Fu, K., et al.: Negating interfacial impedance in garnet-based solid-state Li metal batteries. *Nat. Mater.* **16**, 572–579 (2017). <https://doi.org/10.1038/nmat4821>

18. Choi, S., Jeon, M., Ahn, J., et al.: Quantitative analysis of microstructures and reaction interfaces on composite cathodes in all-solid-state batteries using a three-dimensional reconstruction technique. *ACS Appl. Mater. Inter.* **10**, 23740–23747 (2018)
19. Koerver, R., Aygün, I., Leichtweiß, T., et al.: Capacity fade in solid-state batteries: interphase formation and chemomechanical processes in nickel-rich layered oxide cathodes and lithium thiophosphate solid electrolytes. *Chem. Mater.* **29**, 5574–5582 (2017)
20. Han, F.D., Zhu, Y.Z., He, X.F., et al.: Electrochemical stability of  $\text{Li}_{10}\text{GeP}_2\text{S}_{12}$  and  $\text{Li}_7\text{La}_3\text{Zr}_2\text{O}_{12}$  solid electrolytes. *Adv. Energy Mater.* **6**, 1501590 (2016). <https://doi.org/10.1002/aenm.201501590>
21. Fan, X.L., Ji, X., Han, F.D., et al.: Fluorinated solid electrolyte interphase enables highly reversible solid-state Li metal battery. *Sci. Adv.* (2018). <https://doi.org/10.1126/sciadv.aau9245>
22. Haruyama, J., Sodeyama, K., Han, L.Y., et al.: Space-charge layer effect at interface between oxide cathode and sulfide electrolyte in all-solid-state lithium-ion battery. *Chem. Mater.* **26**, 4248–4255 (2014). <https://doi.org/10.1021/cm5016959>
23. Barton, J., Bockris, J.O.M.: The electrolytic growth of dendrites from ionic solutions. *Proc. R. Soc. Lond. A* **268**, 485–505 (1962). <https://doi.org/10.1098/rspa.1962.0154>
24. Han, F.D., Westover, A.S., Yue, J., et al.: High electronic conductivity as the origin of lithium dendrite formation within solid electrolytes. *Nat. Energy* **4**, 187–196 (2019). <https://doi.org/10.1038/s41560-018-0312-z>
25. Sharafi, A., Kazyak, E., Davis, A.L., et al.: Surface chemistry mechanism of ultra-low interfacial resistance in the solid-state electrolyte  $\text{Li}_7\text{La}_3\text{Zr}_2\text{O}_{12}$ . *Chem. Mater.* **29**, 7961–7968 (2017). <https://doi.org/10.1021/acs.chemmater.7b03002>
26. Wu, J.F., Pu, B.W., Wang, D., et al.: In situ formed shields enabling  $\text{Li}_2\text{CO}_3$ -free solid electrolytes: a new route to uncover the intrinsic lithiophilicity of garnet electrolytes for dendrite-free Li-metal batteries. *ACS Appl. Mater. Inter.* **11**, 898–905 (2019). <https://doi.org/10.1021/acsami.8b18356>
27. Huo, H.Y., Chen, Y., Zhao, N., et al.: In-situ formed  $\text{Li}_2\text{CO}_3$ -free garnet/Li interface by rapid acid treatment for dendrite-free solid-state batteries. *Nano Energy* **61**, 119–125 (2019). <https://doi.org/10.1016/j.nanoen.2019.04.058>
28. Krauskopf, T., Hartmann, H., Zeier, W.G., et al.: Toward a fundamental understanding of the lithium metal anode in solid-state batteries: an electrochemo-mechanical study on the garnet-type solid electrolyte  $\text{Li}_{6.25}\text{Al}_{0.25}\text{La}_3\text{Zr}_2\text{O}_{12}$ . *ACS Appl. Mater. Inter.* **11**, 14463–14477 (2019). <https://doi.org/10.1021/acsami.9b02537>
29. Wang, M., Sakamoto, J.: Correlating the interface resistance and surface adhesion of the Li metal-solid electrolyte interface. *J. Power Sources* **377**, 7–11 (2018). <https://doi.org/10.1016/j.jpowsour.2017.11.078>
30. Wang, J.Y., Wang, H.S., Xie, J., et al.: Fundamental study on the wetting property of liquid lithium. *Energy Storage Mater.* **14**, 345–350 (2018). <https://doi.org/10.1016/j.ensm.2018.05.021>
31. Mugele, F., Baret, J.C.: Electrowetting: from basics to applications. *J. Phys.: Condens. Matter* **17**, 705–774 (2005). <https://doi.org/10.1088/0953-8984/17/28/r01>
32. Persson, B.N.J.: Contact mechanics for randomly rough surfaces. *Surf. Sci. Rep.* **61**, 201–227 (2006). <https://doi.org/10.1016/j.surfrep.2006.04.001>
33. Hlushkou, D., Reising, A.E., Kaiser, N., et al.: The influence of void space on ion transport in a composite cathode for all-solid-state batteries. *J. Power Sources* **396**, 363–370 (2018). <https://doi.org/10.1016/j.jpowsour.2018.06.041>
34. Yamakawa, S., Ohta, S., Kobayashi, T.: Effect of positive electrode microstructure in all-solid-state lithium-ion battery on high-rate discharge capability. *Solid State Ion.* **344**, 115079 (2020). <https://doi.org/10.1016/j.ssi.2019.115079>
35. Froboese, L., van der Sichel, J.F., Loellhoeffel, T., et al.: Effect of microstructure on the ionic conductivity of an all solid-state battery electrode. *J. Electrochem. Soc.* **166**, A318–A328 (2019). <https://doi.org/10.1149/2.0601902jes>
36. Sangrós Giménez, C., Helters, L., Schilde, C., et al.: Modeling the electrical conductive paths within all-solid-state battery electrodes. *Chem. Eng. Technol.* **43**, 819–829 (2020). <https://doi.org/10.1002/ceat.201900501>
37. Kimura, Y., Fakkao, M., Nakamura, T., et al.: Influence of active material loading on electrochemical reactions in composite solid-state battery electrodes revealed by *operando* 3D CT-XANES imaging. *ACS Appl. Energy Mater.* **3**, 7782–7793 (2020)
38. Shi, T., Tu, Q.S., Tian, Y.S., et al.: All-solid-state batteries: high active material loading in all-solid-state battery electrode via particle size optimization. *Adv. Energy Mater.* **10**, 2070004 (2020). <https://doi.org/10.1002/aenm.202070004>
39. Bielefeld, A., Weber, D.A., Janek, J.: Microstructural modeling of composite cathodes for all-solid-state batteries. *J. Phys. Chem. C* **123**, 1626–1634 (2019). <https://doi.org/10.1021/acs.jpcc.8b11043>
40. Liu, T., Zhang, Y.B., Chen, R.J., et al.: Non-successive degradation in bulk-type all-solid-state lithium battery with rigid interfacial contact. *Electrochem. Commun.* **79**, 1–4 (2017). <https://doi.org/10.1016/j.elecom.2017.03.016>
41. Chung, H., Kang, B.: Mechanical and thermal failure induced by contact between a  $\text{Li}_{1.5}\text{Al}_{0.5}\text{Ge}_{1.5}(\text{PO}_4)_3$  solid electrolyte and Li metal in an all solid-state Li cell. *Chem. Mater.* **29**, 8611–8619 (2017). <https://doi.org/10.1021/acs.chemmater.7b02301>
42. Tippens, J., Miers, J.C., Afshar, A., et al.: Visualizing chemo-mechanical degradation of a solid-state battery electrolyte. *ACS Energy Lett.* **4**, 1475–1483 (2019). <https://doi.org/10.1021/acsenerylett.9b00816>
43. Zhu, J.P., Zhao, J., Xiang, Y.X., et al.: Chemomechanical failure mechanism study in NASICON-type  $\text{Li}_{1.3}\text{Al}_{0.3}\text{Ti}_{1.7}(\text{PO}_4)_3$  solid-state lithium batteries. *Chem. Mater.* **32**, 4998–5008 (2020). <https://doi.org/10.1021/acs.chemmater.9b05295>
44. Tian, H.K., Qi, Y.: Simulation of the effect of contact area loss in all-solid-state Li-ion batteries. *J. Electrochem. Soc.* **164**, E3512–E3521 (2017). <https://doi.org/10.1149/2.0481711jes>
45. McGrogan, F.P., Swamy, T., Bishop, S.R., et al.: Compliant yet brittle mechanical behavior of  $\text{Li}_2\text{S}-\text{P}_2\text{S}_5$  lithium-ion-conducting solid electrolyte. *Adv. Energy Mater.* **7**, 1602011 (2017). <https://doi.org/10.1002/aenm.201602011>
46. Bucci, G., Swamy, T., Chiang, Y.M., et al.: Modeling of internal mechanical failure of all-solid-state batteries during electrochemical cycling, and implications for battery design. *J. Mater. Chem. A* **5**, 19422–19430 (2017). <https://doi.org/10.1039/c7ta03199h>
47. Deng, Z., Wang, Z.B., Chu, I.H., et al.: Elastic properties of alkali superionic conductor electrolytes from first principles calculations. *J. Electrochem. Soc.* **163**, A67–A74 (2015). <https://doi.org/10.1149/2.0061602jes>
48. Zhang, W.B., Schröder, D., Arlt, T., et al.: (Electro)chemical expansion during cycling: monitoring the pressure changes in operating solid-state lithium batteries. *J. Mater. Chem. A* **5**, 9929–9936 (2017). <https://doi.org/10.1039/c7ta02730c>
49. Ohta, S., Kobayashi, T., Asaoka, T.: High lithium ionic conductivity in the garnet-type oxide  $\text{Li}_{7-x}\text{La}_3(\text{Zr}_{2-x}\text{Nb}_x)\text{O}_{12}$  ( $x=0-2$ ). *J. Power Sources* **196**, 3342–3345 (2011). <https://doi.org/10.1016/j.jpowsour.2010.11.089>
50. Kamaya, N., Homma, K., Yamakawa, Y., et al.: A lithium superionic conductor. *Nat. Mater.* **10**, 682–686 (2011). <https://doi.org/10.1038/nmat3066>



51. Richards, W.D., Miara, L.J., Wang, Y., et al.: Interface stability in solid-state batteries. *Chem. Mater.* **28**, 266–273 (2016). <https://doi.org/10.1021/acs.chemmater.5b04082>
52. Jalem, R., Morishita, Y., Okajima, T., et al.: Experimental and first-principles DFT study on the electrochemical reactivity of garnet-type solid electrolytes with carbon. *J. Mater. Chem. A* **4**, 14371–14379 (2016). <https://doi.org/10.1039/c6ta04280e>
53. Zhu, Y.Z., He, X.F., Mo, Y.F.: Origin of outstanding stability in the lithium solid electrolyte materials: insights from thermodynamic analyses based on first-principles calculations. *ACS Appl. Mater. Inter.* **7**, 23685–23693 (2015). <https://doi.org/10.1021/acsami.5b07517>
54. Zhu, Y.Z., He, X.F., Mo, Y.F.: First principles study on electrochemical and chemical stability of solid electrolyte–electrode interfaces in all-solid-state Li-ion batteries. *J. Mater. Chem. A* **4**, 3253–3266 (2016). <https://doi.org/10.1039/c5ta08574h>
55. Schwietert, T.K., Arszewska, V.A., Wang, C., et al.: Clarifying the relationship between redox activity and electrochemical stability in solid electrolytes. *Nat. Mater.* **19**, 428–435 (2020). <https://doi.org/10.1038/s41563-019-0576-0>
56. Lin, D.C., Liu, Y.Y., Cui, Y.: Reviving the lithium metal anode for high-energy batteries. *Nat. Nanotechnol.* **12**, 194–206 (2017). <https://doi.org/10.1038/nnano.2017.16>
57. Wenzel, S., Leichtweiss, T., Krüger, D., et al.: Interphase formation on lithium solid electrolytes: an in situ approach to study interfacial reactions by photoelectron spectroscopy. *Solid State Ion.* **278**, 98–105 (2015). <https://doi.org/10.1016/j.ssi.2015.06.001>
58. Li, J.C., Ma, C., Chi, M.F., et al.: Solid electrolyte: the key for high-voltage lithium batteries. *Adv. Energy Mater.* **5**, 1401408 (2015). <https://doi.org/10.1002/aenm.201401408>
59. Schwöbel, A., Hausbrand, R., Jaegermann, W.: Interface reactions between LiPON and lithium studied by in situ X-ray photoemission. *Solid State Ion.* **273**, 51–54 (2015). <https://doi.org/10.1016/j.ssi.2014.10.017>
60. Fingerle, M., Buchheit, R., Siculo, S., et al.: Reaction and space charge layer formation at the LiCoO<sub>2</sub>–LiPON interface: insights on defect formation and ion energy level alignment by a combined surface science–simulation approach. *Chem. Mater.* **29**, 7675–7685 (2017). <https://doi.org/10.1021/acs.chemmater.7b00890>
61. Sang, L.Z., Haasch, R.T., Gewirth, A.A., et al.: Evolution at the solid electrolyte/gold electrode interface during lithium deposition and stripping. *Chem. Mater.* **29**, 3029–3037 (2017). <https://doi.org/10.1021/acs.chemmater.7b00034>
62. Wenzel, S., Weber, D.A., Leichtweiss, T., et al.: Interphase formation and degradation of charge transfer kinetics between a lithium metal anode and highly crystalline Li<sub>7</sub>P<sub>3</sub>S<sub>11</sub> solid electrolyte. *Solid State Ion.* **286**, 24–33 (2016). <https://doi.org/10.1016/j.ssi.2015.11.034>
63. Wu, S.N., Neo, S.S., Dong, Z.L., et al.: Tunable ionic and electronic conduction of lithium nitride via phosphorus and arsenic substitution: a first-principles study. *J. Phys. Chem. C* **114**, 16706–16709 (2010). <https://doi.org/10.1021/jp1045047>
64. Wenzel, S., Randau, S., Leichtweiß, T., et al.: Direct observation of the interfacial instability of the fast ionic conductor Li<sub>10</sub>GeP<sub>2</sub>S<sub>12</sub> at the lithium metal anode. *Chem. Mater.* **28**, 2400–2407 (2016). <https://doi.org/10.1021/acs.chemmater.6b00610>
65. Bron, P., Roling, B., Dehnen, S.: Impedance characterization reveals mixed conducting interphases between sulfidic superionic conductors and lithium metal electrodes. *J. Power Sources* **352**, 127–134 (2017). <https://doi.org/10.1016/j.jpowsour.2017.03.103>
66. Sakuda, A., Hayashi, A., Tatsumisago, M.: Interfacial observation between LiCoO<sub>2</sub> electrode and Li<sub>2</sub>S–P<sub>2</sub>S<sub>5</sub> solid electrolytes of all-solid-state lithium secondary batteries using transmission electron microscopy. *Chem. Mater.* **22**, 949–956 (2010). <https://doi.org/10.1021/cm901819c>
67. Chu, I.H., Nguyen, H., Hy, S., et al.: Insights into the performance limits of the Li<sub>7</sub>P<sub>3</sub>S<sub>11</sub> superionic conductor: a combined first-principles and experimental study. *ACS Appl. Mater. Inter.* **8**, 7843–7853 (2016). <https://doi.org/10.1021/acsami.6b00833>
68. Haruyama, J., Sodeyama, K., Tateyama, Y.: Cation mixing properties toward Co diffusion at the LiCoO<sub>2</sub> cathode/sulfide electrolyte interface in a solid-state battery. *ACS Appl. Mater. Inter.* **9**, 286–292 (2017). <https://doi.org/10.1021/acsami.6b08435>
69. Zhang, W.B., Richter, F.H., Culver, S.P., et al.: Degradation mechanisms at the Li<sub>10</sub>GeP<sub>2</sub>S<sub>12</sub>/LiCoO<sub>2</sub> cathode interface in an all-solid-state lithium-ion battery. *ACS Appl. Mater. Inter.* **10**, 22226–22236 (2018). <https://doi.org/10.1021/acsami.8b05132>
70. Oh, G., Hirayama, M., Kwon, O., et al.: Bulk-type all solid-state batteries with 5 V class LiNi<sub>0.5</sub>Mn<sub>1.5</sub>O<sub>4</sub> cathode and Li<sub>10</sub>GeP<sub>2</sub>S<sub>12</sub> solid electrolyte. *Chem. Mater.* **28**, 2634–2640 (2016). <https://doi.org/10.1021/acs.chemmater.5b04940>
71. Sumita, M., Tanaka, Y., Ikeda, M., et al.: Charged and discharged states of cathode/sulfide electrolyte interfaces in all-solid-state lithium ion batteries. *J. Phys. Chem. C* **120**, 13332–13339 (2016). <https://doi.org/10.1021/acs.jpcc.6b01207>
72. Zhang, W.B., Leichtweiß, T., Culver, S.P., et al.: The detrimental effects of carbon additives in Li<sub>10</sub>GeP<sub>2</sub>S<sub>12</sub>-based solid-state batteries. *ACS Appl. Mater. Inter.* **9**, 35888–35896 (2017). <https://doi.org/10.1021/acsami.7b11530>
73. Ma, C., Cheng, Y.Q., Yin, K.B., et al.: Interfacial stability of Li metal-solid electrolyte elucidated via in situ electron microscopy. *Nano Lett.* **16**, 7030–7036 (2016). <https://doi.org/10.1021/acs.nanolett.6b03223>
74. Wolfenstine, J., Rangasamy, E., Allen, J.L., et al.: High conductivity of dense tetragonal Li<sub>7</sub>La<sub>3</sub>Zr<sub>2</sub>O<sub>12</sub>. *J. Power Sources* **208**, 193–196 (2012). <https://doi.org/10.1016/j.jpowsour.2012.02.031>
75. Kim, Y., Yoo, A., Schmidt, R., et al.: Electrochemical stability of Li<sub>6.5</sub>La<sub>3</sub>Zr<sub>1.5</sub>M<sub>0.5</sub>O<sub>12</sub> (M = Nb or Ta) against metallic lithium. *Front. Energy Res.* **4**, 20 (2016). <https://doi.org/10.3389/fenrg.2016.00020>
76. Rettenwander, D., Wagner, R., Reyer, A., et al.: Interface instability of Fe-stabilized Li<sub>7</sub>La<sub>3</sub>Zr<sub>2</sub>O<sub>12</sub> versus Li metal. *J. Phys. Chem. C* **122**, 3780–3785 (2018). <https://doi.org/10.1021/acs.jpcc.7b12387>
77. Afyon, S., Krumeich, F., Rupp, J.L.M.: A shortcut to garnet-type fast Li-ion conductors for all-solid state batteries. *J. Mater. Chem. A* **3**, 18636–18648 (2015). <https://doi.org/10.1039/c5ta03239c>
78. Kim, K.H., Iriyama, Y., Yamamoto, K., et al.: Characterization of the interface between LiCoO<sub>2</sub> and Li<sub>7</sub>La<sub>3</sub>Zr<sub>2</sub>O<sub>12</sub> in an all-solid-state rechargeable lithium battery. *J. Power Sources* **196**, 764–767 (2011). <https://doi.org/10.1016/j.jpowsour.2010.07.073>
79. Vardar, G., Bowman, W.J., Lu, Q.Y., et al.: Structure, chemistry, and charge transfer resistance of the interface between Li<sub>7</sub>La<sub>3</sub>Zr<sub>2</sub>O<sub>12</sub> electrolyte and LiCoO<sub>2</sub> cathode. *Chem. Mater.* **30**, 6259–6276 (2018). <https://doi.org/10.1021/acs.chemmater.8b01713>
80. Zarabian, M., Bartolini, M., Pereira-Almao, P., et al.: X-ray photoelectron spectroscopy and AC impedance spectroscopy studies of Li–La–Zr–O solid electrolyte thin film/LiCoO<sub>2</sub> cathode interface for all-solid-state Li batteries. *J. Electrochem. Soc.* **164**, A1133–A1139 (2017). <https://doi.org/10.1149/2.0621706jes>
81. Wakasugi, J., Munakata, H., Kanamura, K.: Thermal stability of various cathode materials against Li<sub>6.25</sub>Al<sub>0.25</sub>La<sub>3</sub>Zr<sub>2</sub>O<sub>12</sub> electrolyte. *Electrochemistry* **85**, 77–81 (2017). <https://doi.org/10.5796/electrochemistry.85.77>
82. Miara, L., Windmüller, A., Tsai, C.L., et al.: About the compatibility between high voltage spinel cathode materials and solid oxide electrolytes as a function of temperature. *ACS Appl. Mater.*

- Inter. **8**, 26842–26850 (2016). <https://doi.org/10.1021/acsami.6b09059>
83. Klingler, M., Chu, W.F., Weppner, W.: Coulometric titration of substituted  $\text{Li}_x\text{La}_{(2-x)/3}\text{TiO}_3$ . *Ionics* **3**, 289–291 (1997). <https://doi.org/10.1007/BF02375631>
  84. Kotobuki, M., Suzuki, Y., Munakata, H., et al.: Compatibility of  $\text{LiCoO}_2$  and  $\text{LiMn}_2\text{O}_4$  cathode materials for  $\text{Li}_{0.55}\text{La}_{0.35}\text{TiO}_3$  electrolyte to fabricate all-solid-state lithium battery. *J. Power Sources* **195**, 5784–5788 (2010). <https://doi.org/10.1016/j.jpowsour.2010.03.004>
  85. Hartmann, P., Leichtweiss, T., Busche, M.R., et al.: Degradation of NASICON-type materials in contact with lithium metal: formation of mixed conducting interphases (MCI) on solid electrolytes. *J. Phys. Chem. C* **117**, 21064–21074 (2013). <https://doi.org/10.1021/jp4051275>
  86. Wu, B.B., Wang, S.Y., Lochala, J., et al.: The role of the solid electrolyte interphase layer in preventing Li dendrite growth in solid-state batteries. *Energy Environ. Sci.* **11**, 1803–1810 (2018). <https://doi.org/10.1039/c8ee00540k>
  87. Kim, H.S., Oh, Y., Kang, K.H., et al.: Characterization of sputter-deposited  $\text{LiCoO}_2$  thin film grown on NASICON-type electrolyte for application in all-solid-state rechargeable lithium battery. *ACS Appl. Mater. Inter.* **9**, 16063–16070 (2017). <https://doi.org/10.1021/acsami.6b15305>
  88. Wang, S., Bai, Q., Nolan, A.M., et al.: Lithium chlorides and bromides as promising solid-state chemistries for fast ion conductors with good electrochemical stability. *Angew. Chem. Int. Ed.* **58**, 8039–8043 (2019). <https://doi.org/10.1002/anie.201901938>
  89. Pang, Y.P., Wang, X.T., Shi, X.X., et al.: Solid-state prelithiation enables high-performance Li–Al–H anode for solid-state batteries. *Adv. Energy Mater.* **10**, 1902795 (2020). <https://doi.org/10.1002/aenm.201902795>
  90. Zhu, M.F., Pang, Y.P., Lu, F.Q., et al.: In situ formed Li–B–H complex with high Li-ion conductivity as a potential solid electrolyte for Li batteries. *ACS Appl. Mater. Inter.* **11**, 14136–14141 (2019). <https://doi.org/10.1021/acsami.9b01326>
  91. Takahashi, K., Hattori, K., Yamazaki, T., et al.: All-solid-state lithium battery with  $\text{LiBH}_4$  solid electrolyte. *J. Power Sources* **226**, 61–64 (2013). <https://doi.org/10.1016/j.jpowsour.2012.10.079>
  92. Kim, S., Harada, K., Toyama, N., et al.: Room temperature operation of all-solid-state battery using a closo-type complex hydride solid electrolyte and a  $\text{LiCoO}_2$  cathode by interfacial modification. *J. Energy Chem.* **43**, 47–51 (2020). <https://doi.org/10.1016/j.jechem.2019.08.007>
  93. Shi, X., Pang, Y., Wang, B., et al.: In situ forming LiF nano-decorated electrolyte/electrode interfaces for stable all-solid-state batteries. *Mater. Today Nano* **10**, 100079 (2020). <https://doi.org/10.1016/j.mtnano.2020.100079>
  94. Park, K., Goodenough, J.B.: Dendrite-suppressed lithium plating from a liquid electrolyte via wetting of  $\text{Li}_3\text{N}$ . *Adv. Energy Mater.* **7**, 1700732 (2017). <https://doi.org/10.1002/aenm.201700732>
  95. Takada, K., Ohta, N., Zhang, L.Q., et al.: Interfacial phenomena in solid-state lithium battery with sulfide solid electrolyte. *Solid State Ion.* **225**, 594–597 (2012). <https://doi.org/10.1016/j.ssi.2012.01.009>
  96. Takada, K., Ohta, N., Zhang, L.Q., et al.: Interfacial modification for high-power solid-state lithium batteries. *Solid State Ion.* **179**, 1333–1337 (2008). <https://doi.org/10.1016/j.ssi.2008.02.017>
  97. Gittleson, F.S., El Gabaly, F.: Non-faradaic  $\text{Li}^+$  migration and chemical coordination across solid-state battery interfaces. *Nano Lett.* **17**, 6974–6982 (2017). <https://doi.org/10.1021/acs.nanolett.7b03498>
  98. Cheng, Z., Liu, M., Ganapathy, S., et al.: Revealing the impact of space-charge layers on the Li-ion transport in all-solid-state batteries. *Joule* **4**, 1311–1323 (2020). <https://doi.org/10.1016/j.joule.2020.04.002>
  99. Yamamoto, K., Iriyama, Y., Asaka, T., et al.: Dynamic visualization of the electric potential in an all-solid-state rechargeable lithium battery. *Angew. Chem. Int. Ed.* **49**, 4414–4417 (2010). <https://doi.org/10.1002/anie.200907319>
  100. Masuda, H., Ishida, N., Ogata, Y., et al.: Internal potential mapping of charged solid-state-lithium ion batteries using in situ Kelvin probe force microscopy. *Nanoscale* **9**, 893–898 (2017). <https://doi.org/10.1039/c6nr07971g>
  101. de Klerk, N.J., Wagemaker, M.: Space-charge layers in all-solid-state batteries; important or negligible? *ACS Appl. Energy Mater.* **1**, 5609–5618 (2018). <https://doi.org/10.1021/acs.aem.8b01141>
  102. Gao, B., Jalem, R., Ma, Y.M., et al.:  $\text{Li}^+$  transport mechanism at the heterogeneous cathode/solid electrolyte interface in an all-solid-state battery via the first-principles structure prediction scheme. *Chem. Mater.* **32**, 85–96 (2020). <https://doi.org/10.1021/acs.chemmater.9b02311>
  103. Tsai, C.L., Roddatis, V., Chandran, C.V., et al.:  $\text{Li}_7\text{La}_3\text{Zr}_2\text{O}_{12}$  interface modification for Li dendrite prevention. *ACS Appl. Mater. Inter.* **8**, 10617–10626 (2016). <https://doi.org/10.1021/acsami.6b00831>
  104. Kasemchainan, J., Zekoll, S., Spencer Jolly, D., et al.: Critical stripping current leads to dendrite formation on plating in lithium anode solid electrolyte cells. *Nat. Mater.* **18**, 1105–1111 (2019). <https://doi.org/10.1038/s41563-019-0438-9>
  105. Krauskopf, T., Mogwitz, B., Rosenbach, C., et al.: Diffusion limitation of lithium metal and Li–Mg alloy anodes on LLZO type solid electrolytes as a function of temperature and pressure. *Adv. Energy Mater.* **9**, 1902568 (2019). <https://doi.org/10.1002/aenm.201902568>
  106. Shen, F.Y., Dixit, M.B., Xiao, X.H., et al.: Effect of pore connectivity on Li dendrite propagation within LLZO electrolytes observed with synchrotron X-ray tomography. *ACS Energy Lett.* **3**, 1056–1061 (2018). <https://doi.org/10.1021/acsenenergyl.8b00249>
  107. Cheng, E.J., Sharafi, A., Sakamoto, J.: Intergranular Li metal propagation through polycrystalline  $\text{Li}_{6.25}\text{Al}_{0.25}\text{La}_3\text{Zr}_2\text{O}_{12}$  ceramic electrolyte. *Electrochim. Acta* **223**, 85–91 (2017). <https://doi.org/10.1016/j.electacta.2016.12.018>
  108. Yu, S., Siegel, D.J.: Grain boundary contributions to Li-ion transport in the solid electrolyte  $\text{Li}_7\text{La}_3\text{Zr}_2\text{O}_{12}$  (LLZO). *Chem. Mater.* **29**, 9639–9647 (2017). <https://doi.org/10.1021/acs.chemmater.7b02805>
  109. Ma, C., Chen, K., Liang, C.D., et al.: Atomic-scale origin of the large grain-boundary resistance in perovskite Li-ion-conducting solid electrolytes. *Energy Environ. Sci.* **7**, 1638 (2014). <https://doi.org/10.1039/c4ee00382a>
  110. Yu, S., Siegel, D.J.: Grain boundary softening: a potential mechanism for lithium metal penetration through stiff solid electrolytes. *ACS Appl. Mater. Inter.* **10**, 38151–38158 (2018). <https://doi.org/10.1021/acsami.8b17223>
  111. Pesci, F.M., Brugge, R.H., Hekselman, A.K.O., et al.: Elucidating the role of dopants in the critical current density for dendrite formation in garnet electrolytes. *J. Mater. Chem. A* **6**, 19817–19827 (2018). <https://doi.org/10.1039/c8ta08366e>
  112. Swamy, T., Park, R., Sheldon, B.W., et al.: Lithium metal penetration induced by electrodeposition through solid electrolytes: example in single-crystal  $\text{Li}_6\text{La}_3\text{ZrTaO}_{12}$  garnet. *J. Electrochem. Soc.* **165**, A3648–A3655 (2018). <https://doi.org/10.1149/2.1391814jes>
  113. Kazyak, E., Garcia-Mendez, R., LePage, W.S., et al.: Li penetration in ceramic solid electrolytes: *operando* microscopy analysis

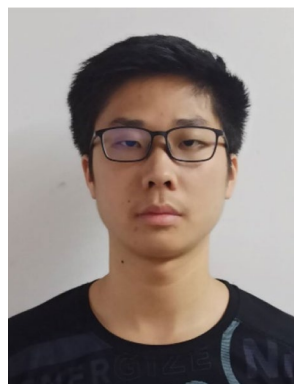
- of morphology, propagation, and reversibility. *Matter* **2**, 1025–1048 (2020). <https://doi.org/10.1016/j.matt.2020.02.008>
114. Porz, L., Swamy, T., Sheldon, B.W., et al.: Mechanism of lithium metal penetration through inorganic solid electrolytes. *Adv. Energy Mater.* **7**, 1701003 (2017). <https://doi.org/10.1002/aenm.201701003>
  115. Zhang, L.Q., Yang, T.T., Du, C.C., et al.: Lithium whisker growth and stress generation in an in situ atomic force microscope-environmental transmission electron microscope set-up. *Nat. Nanotechnol.* **15**, 94–98 (2020). <https://doi.org/10.1038/s41565-019-0604-x>
  116. Aguesse, F., Manalastas, W., Buannic, L., et al.: Investigating the dendritic growth during full cell cycling of garnet electrolyte in direct contact with Li metal. *ACS Appl. Mater. Inter.* **9**, 3808–3816 (2017). <https://doi.org/10.1021/acsami.6b13925>
  117. Ping, W.W., Wang, C.W., Lin, Z.W., et al.: Reversible short-circuit behaviors in garnet-based solid-state batteries. *Adv. Energy Mater.* **10**, 2000702 (2020). <https://doi.org/10.1002/aenm.20200702>
  118. Tian, H.K., Xu, B., Qi, Y.: Computational study of lithium nucleation tendency in  $\text{Li}_7\text{La}_3\text{Zr}_2\text{O}_{12}$  (LLZO) and rational design of interlayer materials to prevent lithium dendrites. *J. Power Sources* **392**, 79–86 (2018). <https://doi.org/10.1016/j.jpowsour.2018.04.098>
  119. Tian, H.K., Liu, Z., Ji, Y.Z., et al.: Interfacial electronic properties dictate Li dendrite growth in solid electrolytes. *Chem. Mater.* **31**, 7351–7359 (2019). <https://doi.org/10.1021/acs.chemmater.9b01967>
  120. Luo, W., Gong, Y.H., Zhu, Y.Z., et al.: Transition from superlithiophobicity to superlithiophilicity of garnet solid-state electrolyte. *J. Am. Chem. Soc.* **138**, 12258–12262 (2016). <https://doi.org/10.1021/jacs.6b06777>
  121. Luo, W., Gong, Y.H., Zhu, Y.Z., et al.: Reducing interfacial resistance between garnet-structured solid-state electrolyte and Li-metal anode by a germanium layer. *Adv. Mater.* **29**, 1606042 (2017). <https://doi.org/10.1002/adma.201606042>
  122. Fu, K., Gong, Y., Fu, Z., et al.: Transient behavior of the metal interface in lithium metal-garnet batteries. *Angew. Chem. Int. Ed.* **56**, 14942–14947 (2017)
  123. Shao, Y., Wang, H., Gong, Z., et al.: Drawing a soft interface: an effective interfacial modification strategy for garnet-type solid-state Li batteries. *ACS Energy Lett.* **3**, 1212–1218 (2018)
  124. Huo, H.Y., Chen, Y., Li, R.Y., et al.: Design of a mixed conductive garnet/Li interface for dendrite-free solid lithium metal batteries. *Energy Environ. Sci.* **13**, 127–134 (2020). <https://doi.org/10.1039/c9ee01903k>
  125. Zhong, Y.R., Xie, Y.J., Hwang, S., et al.: A highly efficient all-solid-state lithium/electrolyte interface induced by an energetic reaction. *Angew. Chem. Int. Ed.* **59**, 14003–14008 (2020). <https://doi.org/10.1002/anie.202004477>
  126. Shi, K., Wan, Z.P., Yang, L., et al.: In situ construction of an ultra-stable conductive composite interface for high-voltage all-solid-state lithium metal batteries. *Angew. Chem. Int. Ed.* **59**, 11784–11788 (2020). <https://doi.org/10.1002/anie.202000547>
  127. Huang, Y., Chen, B., Duan, J., et al.: Graphitic carbon nitride ( $\text{g-C}_3\text{N}_4$ ): an interface enabler for solid-state lithium metal batteries. *Angew. Chem. Int. Ed.* **59**, 3699–3704 (2020). <https://doi.org/10.1002/anie.201914417>
  128. Inoue, Y., Suzuki, K., Matsui, N., et al.: Synthesis and structure of novel lithium-ion conductor  $\text{Li}_7\text{Ge}_3\text{PS}_{12}$ . *J. Solid State Chem.* **246**, 334–340 (2017). <https://doi.org/10.1016/j.jssc.2016.12.001>
  129. Liu, G.Z., Xie, D.J., Wang, X.L., et al.: High air-stability and superior lithium ion conduction of  $\text{Li}_{3+3x}\text{P}_{1-x}\text{Zn}_x\text{S}_{4-x}\text{O}_x$  by aliovalent substitution of ZnO for all-solid-state lithium batteries. *Energy Storage Mater.* **17**, 266–274 (2019). <https://doi.org/10.1016/j.ensm.2018.07.008>
  130. Xie, D.J., Chen, S.J., Zhang, Z.H., et al.: High ion conductive  $\text{Sb}_2\text{O}_5$ -doped  $\beta\text{-Li}_3\text{PS}_4$  with excellent stability against Li for all-solid-state lithium batteries. *J. Power Sources* **389**, 140–147 (2018). <https://doi.org/10.1016/j.jpowsour.2018.04.021>
  131. Han, F.D., Yue, J., Zhu, X.Y., et al.: Suppressing Li dendrite formation in  $\text{Li}_2\text{S-P}_2\text{S}_5$  solid electrolyte by LiI incorporation. *Adv. Energy Mater.* **8**, 1703644 (2018). <https://doi.org/10.1002/aenm.201703644>
  132. Xu, R.C., Han, F.D., Ji, X., et al.: Interface engineering of sulfide electrolytes for all-solid-state lithium batteries. *Nano Energy* **53**, 958–966 (2018). <https://doi.org/10.1016/j.nanoen.2018.09.061>
  133. Tian, Y.J., Ding, F., Zhong, H., et al.:  $\text{Li}_{6.75}\text{La}_3\text{Zr}_{1.75}\text{Ta}_{0.25}\text{O}_{12}$ @amorphous  $\text{Li}_3\text{OCl}$  composite electrolyte for solid state lithium-metal batteries. *Energy Storage Mater.* **14**, 49–57 (2018). <https://doi.org/10.1016/j.ensm.2018.02.015>
  134. Duan, H., Chen, W.P., Fan, M., et al.: Building an air stable and lithium deposition regulable garnet interface from moderate-temperature conversion chemistry. *Angew. Chem. Int. Ed.* **59**, 12069–12075 (2020). <https://doi.org/10.1002/anie.202003177>
  135. Deng, T., Ji, X., Zhao, Y., et al.: Tuning the anode–electrolyte interface chemistry for garnet-based solid-state Li metal batteries. *Adv. Mater.* **32**, 2000030 (2020). <https://doi.org/10.1002/adma.202000030>
  136. Zhang, Z., Chen, S., Yang, J., et al.: Interface re-engineering of  $\text{Li}_{10}\text{GeP}_2\text{S}_{12}$  electrolyte and lithium anode for all-solid-state lithium batteries with ultralong cycle life. *ACS Appl. Mater. Inter.* **10**, 2556–2565 (2018)
  137. Hou, G., Ma, X., Sun, Q., et al.: Lithium dendrite suppression and enhanced interfacial compatibility enabled by an ex situ SEI on Li anode for LAGP-based all-solid-state batteries. *ACS Appl. Mater. Inter.* **10**, 18610–18618 (2018)
  138. Mo, F.J., Ruan, J.F., Sun, S.X., et al.: Lithium dendrites: inside or outside: origin of lithium dendrite formation of all solid-state electrolytes. *Adv. Energy Mater.* **9**, 1970155 (2019). <https://doi.org/10.1002/aenm.201970155>
  139. Ohta, N., Takada, K., Zhang, L., et al.: Enhancement of the high-rate capability of solid-state lithium batteries by nanoscale interfacial modification. *Adv. Mater.* **18**, 2226–2229 (2006). <https://doi.org/10.1002/adma.200502604>
  140. Yang, J., Huang, B.X., Yin, J.Y., et al.: Structure integrity endowed by a Ti-containing surface layer towards ultrastable  $\text{LiNi}_{0.8}\text{Co}_{0.15}\text{Al}_{0.05}\text{O}_2$  for all-solid-state lithium batteries. *J. Electrochem. Soc.* **163**, A1530–A1534 (2016). <https://doi.org/10.1149/2.0331608jes>
  141. Kitaura, H., Hayashi, A., Tadanaga, K., et al.: Electrochemical performance of all-solid-state lithium secondary batteries with Li–Ni–Co–Mn oxide positive electrodes. *Electrochim. Acta* **55**, 8821–8828 (2010). <https://doi.org/10.1016/j.electacta.2010.07.066>
  142. Kitaura, H., Hayashi, A., Tadanaga, K., et al.: Improvement of electrochemical performance of all-solid-state lithium secondary batteries by surface modification of  $\text{LiMn}_2\text{O}_4$  positive electrode. *Solid State Ion.* **192**, 304–307 (2011). <https://doi.org/10.1016/j.ssi.2010.08.019>
  143. Ohta, N., Takada, K., Sakaguchi, I., et al.:  $\text{LiNbO}_3$ -coated  $\text{LiCoO}_2$  as cathode material for all solid-state lithium secondary batteries. *Electrochem. Commun.* **9**, 1486–1490 (2007). <https://doi.org/10.1016/j.elecom.2007.02.008>
  144. Kato, Y., Hori, S., Saito, T., et al.: High-power all-solid-state batteries using sulfide superionic conductors. *Nat. Energy* **1**, 16030 (2016). <https://doi.org/10.1038/nenergy.2016.30>
  145. Zhang, J., Zhong, H.Y., Zheng, C., et al.: All-solid-state batteries with slurry coated  $\text{LiNi}_{0.8}\text{Co}_{0.1}\text{Mn}_{0.1}\text{O}_2$  composite cathode and  $\text{Li}_6\text{PS}_5\text{Cl}$  electrolyte: effect of binder content. *J. Power Sources* **391**, 73–79 (2018). <https://doi.org/10.1016/j.jpowsour.2018.04.069>



146. Chida, S., Miura, A., Rosero-Navarro, N.C., et al.: Liquid-phase synthesis of  $\text{Li}_6\text{PS}_3\text{Br}$  using ultrasonication and application to cathode composite electrodes in all-solid-state batteries. *Ceram. Int.* **44**, 742–746 (2018). <https://doi.org/10.1016/j.ceramint.2017.09.241>
147. Park, K.H., Oh, D.Y., Choi, Y.E., et al.: Solution-processable glass  $\text{LiI-Li}_4\text{SnS}_4$  superionic conductors for all-solid-state Li-ion batteries. *Adv. Mater.* **28**, 1874–1883 (2016). <https://doi.org/10.1002/adma.201505008>
148. Jung, S.H., Oh, K., Nam, Y.J., et al.:  $\text{Li}_3\text{BO}_3\text{-Li}_2\text{CO}_3$ : rationally designed buffering phase for sulfide all-solid-state Li-ion batteries. *Chem. Mater.* **30**, 8190–8200 (2018). <https://doi.org/10.1021/acs.chemmater.8b03321>
149. Ito, Y., Sakurai, Y., Yubuchi, S., et al.: Application of  $\text{LiCoO}_2$  particles coated with lithium ortho-oxosalt thin films to sulfide-type all-solid-state lithium batteries. *J. Electrochem. Soc.* **162**, A1610–A1616 (2015). <https://doi.org/10.1149/2.0771508jes>
150. Deng, S.X., Li, X., Ren, Z.H., et al.: Dual-functional interfaces for highly stable Ni-rich layered cathodes in sulfide all-solid-state batteries. *Energy Storage Mater.* **27**, 117–123 (2020). <https://doi.org/10.1016/j.ensm.2020.01.009>
151. Xiao, Y.H., Miara, L.J., Wang, Y., et al.: Computational screening of cathode coatings for solid-state batteries. *Joule* **3**, 1252–1275 (2019). <https://doi.org/10.1016/j.joule.2019.02.006>
152. Wan, H.L., Peng, G., Yao, X.Y., et al.:  $\text{Cu}_2\text{ZnSnS}_4$ /graphene nanocomposites for ultrafast, long life all-solid-state lithium batteries using lithium metal anode. *Energy Storage Mater.* **4**, 59–65 (2016). <https://doi.org/10.1016/j.ensm.2016.02.004>
153. Yao, X.Y., Huang, N., Han, F.D., et al.: High-performance all-solid-state lithium-sulfur batteries enabled by amorphous sulfur-coated reduced graphene oxide cathodes. *Adv. Energy Mater.* **7**, 1602923 (2017). <https://doi.org/10.1002/aenm.201602923>
154. Lu, F.Q., Pang, Y.P., Zhu, M.F., et al.: A high-performance Li–B–H electrolyte for all-solid-state Li batteries. *Adv. Funct. Mater.* **29**, 1809219 (2019). <https://doi.org/10.1002/adfm.201809219>
155. Ohta, S., Komagata, S., Seki, J., et al.: All-solid-state lithium ion battery using garnet-type oxide and  $\text{Li}_2\text{BO}_3$  solid electrolytes fabricated by screen-printing. *J. Power Sources* **238**, 53–56 (2013). <https://doi.org/10.1016/j.jpowsour.2013.02.073>
156. Han, F.D., Yue, J., Chen, C., et al.: Interphase engineering enabled all-ceramic lithium battery. *Joule* **2**, 497–508 (2018). <https://doi.org/10.1016/j.joule.2018.02.007>
157. Kitaura, H., Hayashi, A., Ohtomo, T., et al.: Fabrication of electrode–electrolyte interfaces in all-solid-state rechargeable lithium batteries by using a supercooled liquid state of the glassy electrolytes. *J. Mater. Chem.* **21**, 118–124 (2011). <https://doi.org/10.1039/c0jm01090a>
158. Hou, L.P., Yuan, H., Zhao, C.Z., et al.: Improved interfacial electronic contacts powering high sulfur utilization in all-solid-state lithium–sulfur batteries. *Energy Storage Mater.* **25**, 436–442 (2020). <https://doi.org/10.1016/j.ensm.2019.09.037>
159. Kim, D.H., Oh, D.Y., Park, K.H., et al.: Infiltration of solution-processable solid electrolytes into conventional Li-ion-battery electrodes for all-solid-state Li-ion batteries. *Nano Lett.* **17**, 3013–3020 (2017)
160. Li, Y., Cao, D.X., Arnold, W., et al.: Regulated lithium ionic flux through well-aligned channels for lithium dendrite inhibition in solid-state batteries. *Energy Storage Mater.* **31**, 344–351 (2020). <https://doi.org/10.1016/j.ensm.2020.06.029>
161. van den Broek, J., Afyon, S., Rupp, J.L.M.: Interface-engineered all-solid-state Li-ion batteries based on garnet-type fast  $\text{Li}^+$  conductors. *Adv. Energy Mater.* **6**, 1600736 (2016). <https://doi.org/10.1002/aenm.201600736>
162. Xu, S.M., McOwen, D.W., Zhang, L., et al.: All-in-one lithium-sulfur battery enabled by a porous-dense-porous garnet architecture. *Energy Storage Mater.* **15**, 458–464 (2018). <https://doi.org/10.1016/j.ensm.2018.08.009>
163. Li, Q., Yi, T.C., Wang, X.L., et al.: In-situ visualization of lithium plating in all-solid-state lithium-metal battery. *Nano Energy* **63**, 103895 (2019). <https://doi.org/10.1016/j.nanoen.2019.103895>
164. Han, S.Y., Lewis, J.A., Shetty, P.P., et al.: Porous metals from chemical dealloying for solid-state battery anodes. *Chem. Mater.* **32**, 2461–2469 (2020). <https://doi.org/10.1021/acs.chemmater.9b04992>
165. Han, F.D., Gao, T., Zhu, Y.J., et al.: A battery made from a single material. *Adv. Mater.* **27**, 3473–3483 (2015). <https://doi.org/10.1002/adma.201500180>
166. Lee, Y.G., Fujiki, S., Jung, C., et al.: High-energy long-cycling all-solid-state lithium metal batteries enabled by silver-carbon composite anodes. *Nat. Energy* **5**, 299–308 (2020). <https://doi.org/10.1038/s41560-020-0575-z>
167. Zhang, X.Y., Xiang, Q., Tang, S., et al.: Long cycling life solid-state Li metal batteries with stress self-adapted Li/garnet interface. *Nano Lett.* **20**, 2871–2878 (2020). <https://doi.org/10.1021/acs.nanolett.0c00693>



**Yuepeng Pang** received his Ph.D degree in the Department of Materials Science and Engineering at Zhejiang University in 2014. He is now an associate professor in the School of Materials Science and Engineering at the University of Shanghai for Science and Technology. His current research mainly focuses on hydride materials for solid-state batteries.



**Jinyu Pan** received his B.S. degree in the Department of Materials Science and Engineering at Shanghai Maritime University in 2019. Now he is an M.S. student in the School of Materials Science and Engineering at the University of Shanghai for Science and Technology. His research focuses on the interfacial design of solid-state batteries.



**Junhe Yang** received his Ph.D degree from Northeastern University in China. He is now a professor in the University of Shanghai for Science and Technology. His research interests focus on new energy materials, such as graphene, porous carbonaceous materials and nanomaterials. He won the first-class prize of Shanghai Natural Science Award in 2018.



**Shiyong Zheng** respectively, received his B.S., M.S. and Ph.D. degrees in Sichuan University, Zhejiang University and Fudan University. Then, he worked as a visiting researcher in the National Institute of Standards and Technology and the University of Maryland. He is now a professor in the University of Shanghai for Science and Technology. His research interests focus on new energy materials for batteries, supercapacitors and hydrogen storage. He was chosen as “Young and Middle-aged Experts with outstanding Experts” in the New Century Talents Project in 2019.

aged Experts with outstanding Experts” in the New Century Talents Project in 2019.



**Chunsheng Wang** is a Robert Franklin and Frances Riggs Wright Distinguished Chair Professor in the Department of Chemical and Biomolecular Engineering and Chemistry and Biochemistry at the University of Maryland. He is an associate editor of *ACS Applied Energy Materials*, and UMD Director of The UMD-ARL Center for Research in Extreme Batteries. His research focuses on rechargeable batteries. He has published more than 280 papers. Dr. Wang is a Highly Cited

Researcher of 2018 and 2019, with more than 23000 citations and an *H*-index of 80 (ISI).